

The University of Maine

DigitalCommons@UMaine

Honors College

Spring 5-2020

The Microstructural Heterogeneity of Ice in Jarvis Glacier, Alaska

Renée Clavette

University of Maine

Follow this and additional works at: <https://digitalcommons.library.umaine.edu/honors>



Part of the [Glaciology Commons](#)

Recommended Citation

Clavette, Renée, "The Microstructural Heterogeneity of Ice in Jarvis Glacier, Alaska" (2020). *Honors College*. 589.

<https://digitalcommons.library.umaine.edu/honors/589>

This Honors Thesis is brought to you for free and open access by DigitalCommons@UMaine. It has been accepted for inclusion in Honors College by an authorized administrator of DigitalCommons@UMaine. For more information, please contact um.library.technical.services@maine.edu.

THE MICROSTRUCTURAL HETEROGENEITY OF ICE IN
JARVIS GLACIER, ALASKA

by

Renée N. Clavette

A Thesis Submitted in Partial Fulfillment
Of the Requirements for a Degree with Honors
(Earth and Climate Sciences)

The Honors College

University of Maine

May 2020

Advisory Committee:

Christopher Gerbi, Professor of Earth and Climate Sciences, Associate Dean of
Research (NSFA), Advisor

Seth Campbell, Assistant Professor of Earth and Climate Sciences

Scott Johnson, Professor and Director, School of Earth and Climate Sciences

Melissa Ladenheim, Associate Dean of the Honors College

Amanda Olsen, Associate Professor of Earth and Climate Science

ABSTRACT

Glacier ice behaves as a viscous fluid, where flow is controlled by a number of external and internal processes. One crucial, yet sometimes overlooked, factor is ice microstructure. Studies have shown that ice crystal (grain) size, shape, and orientation influence the viscous strength of ice, and therefore its resistance to flow and deformation. Glacier flow is also impacted by friction at the bed and lateral margins. The magnitude of flow resistance due to the lateral margins is not well quantified. The goal of this overall project is to evaluate how heterogeneous optical properties of ice are that are influenced by strain. Ice cores were drilled in a partial transect across Jarvis Glacier, a small, mountain glacier located in Eastern Alaska. Three ice cores were selected for making thin sections and analyzing under cross-polarized light. They were drilled at different distances from the lateral margin, and therefore should experience varying magnitudes of friction from the margin. Studies show that bubbles can potentially be used as strain markers in ice by examining their elongation and orientations. Using borehole televiewer imagery, larger dipping structures were categorized and their orientations and dip angles plotted. Image analyses of grain size, circularity, bubble shape and orientation indicate that these properties are heterogeneous between ice cores. Heterogeneity among these measurements suggests that flow models may need to adjust to incorporate the intricate and important impacts that grain and subgrain processes have on ice dynamics such as flow magnitude.

ACKNOWLEDGEMENTS

I would like to thank my advisor Dr. Chris Gerbi, for his support and for encouraging me to grow my project from sophomore year into this Honors Thesis. I appreciate him always being willing to answer my questions and give me advice over these past three years. I would also like to acknowledge all of the people in the overarching Jarvis Project from the University of Maine, Dartmouth College, and University of Alaska, Fairbanks, whose data were crucial to this project and my overall understanding of the region. Especially, I thank Stephanie Mills for her ice thin section work, which is included in this project, and for teaching me how to conduct research in the ice core freezer. Also, Kate Hruby, whose figure is included in this thesis, for providing me mentorship from a graduate student perspective. Thank you to the remainder of my thesis committee, Dr. Seth Campbell, Dr. Scott Johnson, Dr. Melissa Ladenheim, and Dr. Amanda Olsen. Without their suggestions and support, this thesis would not have been possible. Overall, I wouldn't have been successful in this process without the support of my friends and family. I especially want to acknowledge my roommates for allowing me to stress clean the apartment before my defense and helping me set up my room to defend remotely on Zoom. There's no group of people I'd rather be in quarantine with these past couple of months! This project was funded by National Science Foundation grant PLR-1503924 as well as the Thomas E. Lynch Honors Thesis Scholarship, which I appreciate immensely.

TABLE OF CONTENTS

INTRODUCTION	1
SCIENTIFIC BACKGROUND	4
METHODS	9
Area of Study and Sample Collection	9
Optical Televiewer	11
Thin Sections	13
Image Analysis	16
Rose Diagrams	19
Statistical Plots	20
RESULTS	21
Televiewer Feature Orientation	21
Bubble Orientation	22
Grain Size	25
Grain Circularity	29
Bubble Shape (Aspect Ratio)	34
DISCUSSION	39
Intrahole Heterogeneity	39
Interhole Heterogeneity	45
Implications for Glacier Mechanics	49
CONCLUSIONS	52
REFERENCES	54
APPENDIX: Table of Grain Size, Grain Circularity, and Bubble Aspect Ratio	56
AUTHOR'S BIOGRAPHY	57

LIST OF FIGURES

Figure 1: Map of Jarvis Glacier Location	10
Figure 2: Optical Televiewer Image	12
Figure 3: Set-up for Taking Photographs of Thin Sections	15
Figure 4: Images of Thin Sections	15
Figure 5: Example Thin Section with Grain and Bubble Outlines	18
Figure 6: Stereonet Plot of Dipping Structures	21
Figure 7: Stereonet Rose Diagram of Sample JA35 Bubble Orientation	23
Figure 8: Stereonet Rose Diagram of Sample JB32 Bubble Orientation	23
Figure 9: Stereonet Rose Diagram of Sample JE10 Bubble Orientation	24
Figure 10: Master Histograms of Grain Size	26
Figure 11: Representative Histograms of Grain Size	27
Figure 12: Line Graph of Core-JA Grain Size	27
Figure 13: Line Graph of Core-JB Grain Size	28
Figure 14: Line Graph of Core-JE Grain Size	28
Figure 15: Master Histograms of Grain Circularity	30
Figure 16: Representative Histograms of Grain Circularity	31
Figure 17: Line Graph of Core-JA Grain Circularity	32
Figure 18: Line Graph of Core-JB Grain Circularity	32
Figure 19: Line Graph of Core-JE Grain Circularity	33
Figure 20: Master Histograms of Bubble Aspect Ratio	35
Figure 21: Representative Histograms of Bubble Aspect Ratio	36
Figure 22: Line Graph of Core-JA Bubble Aspect Ratio	37
Figure 23: Line Graph of Core-JB Bubble Aspect Ratio	37
Figure 24: Line Graph of Core-JE Bubble Aspect Ratio	38
Figure 25: Average Grain Sizes	42
Figure 26: Average Grain Circularity Values	43
Figure 27: Average Bubble Aspect Ratios	44
Figure 28: Stereonet Comparison Plot	48

LIST OF TABLES

Table 1: ImageJ Measurements	17
Table 2: Mean Grain Size, Grain Circularity, and Bubble Aspect Ratio	56

INTRODUCTION

Changes in the cryosphere, or the portion of Earth's surface that is frozen water, have significant environmental and societal impacts. These impacts include sea-level rise, reduced albedo, water supply loss for communities, a potential increase in glacial lake outburst floods, and the release of harmful anthropogenic chemicals. Meltwater draining into the ocean raises sea level, endangering coastal communities and infrastructure. Loss of ice also reduces the planet's overall ability to reflect longwave radiation, or its albedo, creating a positive feedback loop in the Earth system. Societally, glacier meltwater provides a drinking water source, meaning many communities are located in the watersheds of alpine glaciers. Rapid loss of mountain glaciers jeopardizes these communities' water supplies and leads to catastrophic outburst floods from glacial melt. This melt also has the potential to release harmful organochlorine pollutants into water systems, (Miner et al. 2018).

Approximately 69% of all freshwater on Earth is stored in glaciers, as well as ice sheets, shelves, and streams (Gleick 1996). Although most of this mass is located in the major ice sheets, East and West Antarctica and Greenland, alpine glaciers are melting faster, with Alaskan glaciers contributing a significant amount to sea level rise (Zemp et al. 2017). For example, the Tanana River watershed, located in Interior Alaska has experienced a 12% ice cover reduction in the past 60 years (O'Neel et. al. 2014). Glacier mass balance is the net amount of ice gain (accumulation) and ice loss (ablation) over a yearlong period. Accumulation is mainly the result of local precipitation and the overall climate of a region, but can also occur from valley wall avalanches that deposit snow on the glacier surface (Benn & Evans 2010). Ablation occurs through melt, sublimation, or

calving. Other factors that affect ablation include debris cover, geothermal heating, and water content.

Mass changes in the cryosphere can be propagated by ice flow itself. Glacier flow is responsible for transporting mass from the higher altitude accumulation zone to the lower ablation zone, so the velocity of flow and factors that affect it are important to overall mass balance. A glacier with higher flow velocity will transport ice downstream much faster to lower elevations, where melting will occur. Since ice flow controls a glacier system's mass balance "health," a better understanding of flow may help to predict and mitigate the ramifications of glacier loss described previously. Mechanical properties of ice control how glaciers, ice sheets, ice shelves, and ice streams respond to climate forcing. Mechanics result from microstructural and environmental conditions.

Flow rates are controlled by accumulation driven by weather and climate, glacier channel conditions such as water present at the bed or deformability of the underlying sediment, and the flow resistance provided by the lateral margins which may be more significant than flow resistance from the ice itself. Creep, or glacier deformation, is controlled by temperature, water content, debris content, as well as grain size, orientation, and shape. How these factors differ, or their heterogeneity, indicates that deformation occurs at different rates and magnitudes throughout a glacier. This project investigates the heterogeneity of microscale ice properties, by analyzing the grain size, circularity, orientation, and bubble shape and orientation in ice thin sections made from cores taken from a transect across Jarvis Glacier, Alaska. Larger scale features such as clear ice and debris bands were also compared in two of these cores.

The heterogeneity of these factors may significantly influence overall ice strength and therefore flow, so the degree that heterogeneity affects creep must be evaluated further. Heterogeneous ice properties across both vertical and horizontal gradients imply the need for further research in this field, as most flow models assume uniformly deforming ice and use equations with mostly laboratory-derived values.

SCIENTIFIC BACKGROUND

Glaciers are channelized streams of ice with gravity driven flow. Resisting forces include internal viscosity of the ice and friction when sliding occurs. In general, ice dynamics are controlled by boundary conditions as well as internal ice properties that affect flow resistance. Boundary conditions include friction at the glacier bed or lateral margins and the overall impact of its environmental setting. In the subglacial regime, water below the glacier lubricates the bed, reducing friction and inducing basal sliding. This occurs in glaciers that are either temperate, polythermal, or both, as there must be liquid water present. Flow in glaciers that terminate much lower in altitude than their heads may be controlled by creep in the higher elevation, where a frozen bed would persist, but experience basal slip where temperatures are warm enough for liquid water to exist at the bed, (Rabus & Echelmeyer 1997).

Not only is water crucial for channel friction, but the bed material itself can affect friction through its deformability. For instance, softer, sedimentary material can deform under lower stresses than bedrock thus providing less resistance to ice flow. The lateral margins also resist flow, however, the effect at which they do is poorly quantified and understood, (Raymond et. al. 2001). One study found that a glacier with little drag at the bed was greatly resisted by lateral margins, (Whillans & van der Veen, 1997). Under sliding conditions, friction is generated at the lateral margins as well. Local environmental conditions also have a role in ice dynamics due to their effects on mass balance. Since glaciers flow under their own weight and temperature and precipitation mainly control mass balance, weather patterns themselves impact flow.

Internal mechanisms affecting ice dynamics include englacial hydrology and ice strength. Ice strength, as well as ice strength gradients, influence glacier deformation, or creep. Deformation of crystalline materials occurs through different mechanisms. Creep is a grain-scale process resulting from slipping between crystals, and is controlled by temperature, crystal structure and debris inclusions, (Benn & Evans 2010). Similar to quartz, ice crystallizes in hexagonal sheets, referred to as basal planes, that make up a crystal lattice. In ice, however, these basal planes are much weaker, making ice a more deformable material than quartz. Slipping along these planes can be between 100 and 1000 times easier than in other directions, (Hooke, 2005). In some cases, elastic deformation dominates resulting in the lattice structure returning back to its original shape. However, another type of intracrystalline deformation, dislocation glide, results in a change in lattice shape (Passchier & Trouw, 1996). A dislocation occurs in a lattice structure when there are missing or extra points in the structure. The dislocation will migrate through the lattice resulting in an organization storing the least amount of potential energy. This alters the overall shape of the lattice, yet may not result in mechanical fracturing of the ice. Dynamic recrystallization is another grain-scale process related to creep. It is the process in which grain boundaries migrate to produce a lattice structure with the least amount of potential energy. The rate at which this occurs increases with increasing temperature (Passchier & Trouw, 1996)

Basal plane slipping, dislocation glide, and dynamic recrystallization are influenced by conditions at the grain and sub-grain scale, such as grain size, shape, and c-axis orientation (Hooke, 2005, Faria et al. 2014). Grain size, orientation, and shape may indicate the latest strain history of ice, (Hudleston 2015, other). In general, grain size

decreases with strain. However, larger grains are expected deeper in the core since they have had more time to grow and would experience greater temperature at depth due to pressure. Grain orientation influences deformation through the development of a preferred crystallographic orientation during strain. A crystal's c-axis, another term being the optical axis, is perpendicular to its basal plane. During creep, a preferred orientation of c-axes, or fabric, develops (Hudleston, 2015). C-axis orientation not only records strain through its preferred orientation, but affects deformation rates. When these orient in the same direction, known as anisotropy, ice creep can occur at faster rates, (Benn & Evans, 2010). Grain shape is also a factor in this process. Deformation leads to less hexagonal grains with more jagged edges. However, through recrystallization, grain boundary area reduction (GBAR) occurs (Passchier & Trouw 1996). Since grain boundaries themselves possess high internal energy, reducing the total length of boundaries lowers the overall potential energy.

Bubbles form within glaciers through the process of snow melting and refreezing trapping air pockets. As the snow compacts it traps air bubbles that are nearly spherical, however the shapes change as a result of ice deformation. Fegyveresi et al. (2019) found that bubble elongation occurs parallel to the grain's basal plane indicating that it is a deformation driven process. Because of this, bubbles could potentially be used as strain markers, especially on the microscale. Bubbles, especially larger bubbles, deform faster than surrounding ice by a factor of $\sim 5/3$, meaning that smaller strain gradients can still be observed (Alley & Fitzpatrick, 1999). Other studies show that bubbles elongate and orient themselves parallel to glacier flow (Nakawo & Wakahama, 1981, Hudleston 1977, Fegyveresi et al. 2019).

Grain-scale properties and processes are nearly impossible to observe in real time in a glacier, so laboratory experiments are commonly performed to determine the effects of different pressure and temperature conditions on microstructure. For example, Rob & Baker (1978) applied stress, using a uniaxial compression apparatus, to a synthetic ice sample and measured the subsequent strain and grain size. They found that grain size played a large role in creep rate for the samples. Other studies include concentrations of debris to measure the degree of grain boundary migration and creep (Song et al. 2004, 2008). Although laboratory studies are necessary for making smaller scale observations, some cases show that glacier ice is stronger than laboratory ice, so field data should be further incorporated and used to validate laboratory data (Hooke, 1981).

Flow models are essential to predict how glaciers will flow and thus the impacts of climate forcing on glacier mass balance. Glacier flow is characterized by the driving stresses and resisting forces such as channel friction and viscous strength. Glen's Flow Law is generally used to model the relationship between strain rate and stress. Glen's Flow Law: $\dot{\epsilon} = A\tau^n$ which relates strain rate ($\dot{\epsilon}$), or the rate that creep occurs at, to stress (τ). A value of 3 is usually used as the n-exponent, which is supported in laboratory studies, however some field data point to values between 4 and 6 (Hooke 1981). The A-constant relies on various properties such as temperature, grain size, crystallographic orientation, and debris (Glen 1954, Cuffey & Paterson 2010, Hooke 1981). To simplify models, the A-constant is generally attributed only to temperature (Placidi et al. 2010). Isotropic ice, or ice with randomly oriented c-axes, is also assumed. As discussed, ice strength is dependent on microstructure, yet is not generally included in flow models. Modifications to Glen's Flow Law exist which incorporate some microstructural factors

(Hooke 1981). However, they require better constraints from field data and further testing (Placidi et al. 2010). Important field measurements include the spatial distribution of microstructural features. Advancing ice flow laws relies on microstructure data from the field as well as determining how heterogeneous these properties are within ice on small and large scales.

METHODS

Area of Study/Sample Collection

Jarvis Glacier is a temperate glacier located in the Eastern Alaska Range (Fig.1) and was selected due to its relatively simple bed geometry, and accessibility Jarvis Glacier is about 8km long and has a maximum ice thickness of ~220m. It is shallow enough to collect surface to bed cores in multiple locations in one season. Two surface to bed cores were extracted from Jarvis over an approximately 100m distance perpendicular to flow, with three more partial cores collected. They were drilled with a 3” Badger-Eclipse Drill in the summer-2017 field season. In order to reduce the amount of crystallographic change in the ice as a result of fluctuating temperature, the cores were kept at -20.0°C immediately following extraction and processing. Images of all core segments were taken and logged in Fairbanks, AK, by Stephanie Mills. Some of the cores or core segments were shipped to the University of Maine. The boreholes themselves were imaged using an optical televiewer lowered into the holes.

The naming scheme for all samples includes the core and numbered segment that was drilled. Numbers are sequential with increasing depth. Some core segments are made up of multiple parts due to them breaking during handling, in which case they are hyphenated with the number sub-segment. In samples where multiple thin sections were made for a singular core segment an “a” and its corresponding number are added. For example, JB46-1a2 shows that it is the second thin section made for the first sub-segment in core JB: segment 46.

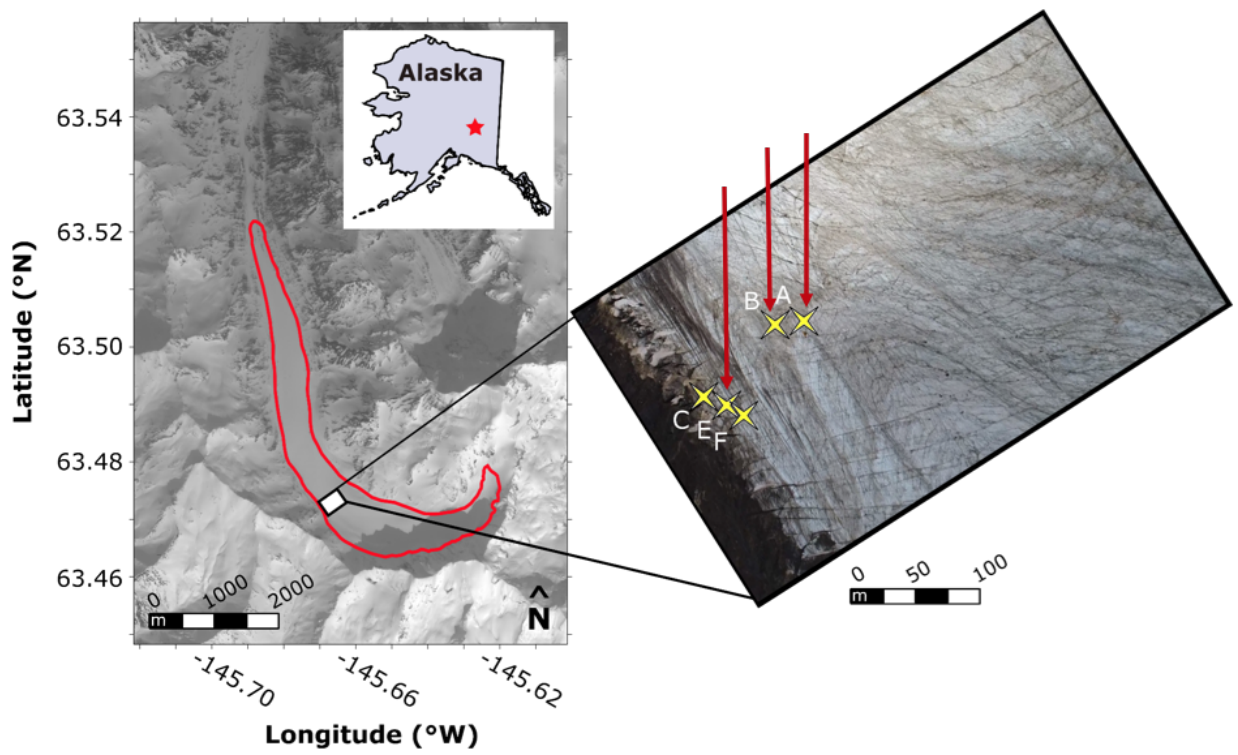


Figure 1

Map image showing the location of Jarvis glacier in Eastern Alaska and the boreholes drilled. The pop-out image shows the area studied with yellow stars placed at boreholes drilled for the overarching project. The red arrows point to cores JA, JB, and JE, which are the subjects of this project. The left side of the pop-out image shows the west lateral margin of the glacier (Image by Kate Hruby).

Optical Televiewer

Televiewer instruments are often used to image borehole walls after a core is extracted. In the field an optical televiewer was lowered into each borehole, taking a 360° image of the entire hole with a labelled North-direction. The unwrapped 360° images were imported into Adobe Illustrator, where a scale was imposed on it, (Fig.2). Various bands are visible in the televiewer images. In glaciers, these types of layers are sheared as flow occurs resulting in dipping bands. The heterogeneity of these structures across cores may also indicate the magnitude of strain rate gradients across a transect. I omitted all partial structures and only included complete ones with a clear sinusoidal shape.

JE is located closest to the lateral margin and JA is closest to the center of flow in relation, so they were selected for analysis. Using Adobe Illustrator, the dip angle of each band as well as the dip direction determined from the unwrapped image, for cores JA and JE. Sinusoidal features were categorized as clear ice or debris-laden ice and then their dip angles and directions were plotted in the program, Stereonet. Stereonet was developed by Rick Allmendinger and is used in various branches of geology to create stereographic plots to display orientations of dipping structures. In structural geology, for instance, Stereonet is often used to plot strike and dip in rock formations. A stereographic projection is a circular plot representing a hemisphere intersected by a plane or line. The location that the plane or line intersects the circle represents orientation, and lines indicate the angle at which a plane intersects the projected hemisphere. For example, a line that passes close to the center of the circle would represent a near vertical band. In my graph, however, points were used in substitution for lines, as they show the point at which a line perpendicular to the plane would intersect the hemisphere. The points were

colored and shaped based on the core and which type of structure (bright or dark), making it possible to see distributions and plot all data on one graph.

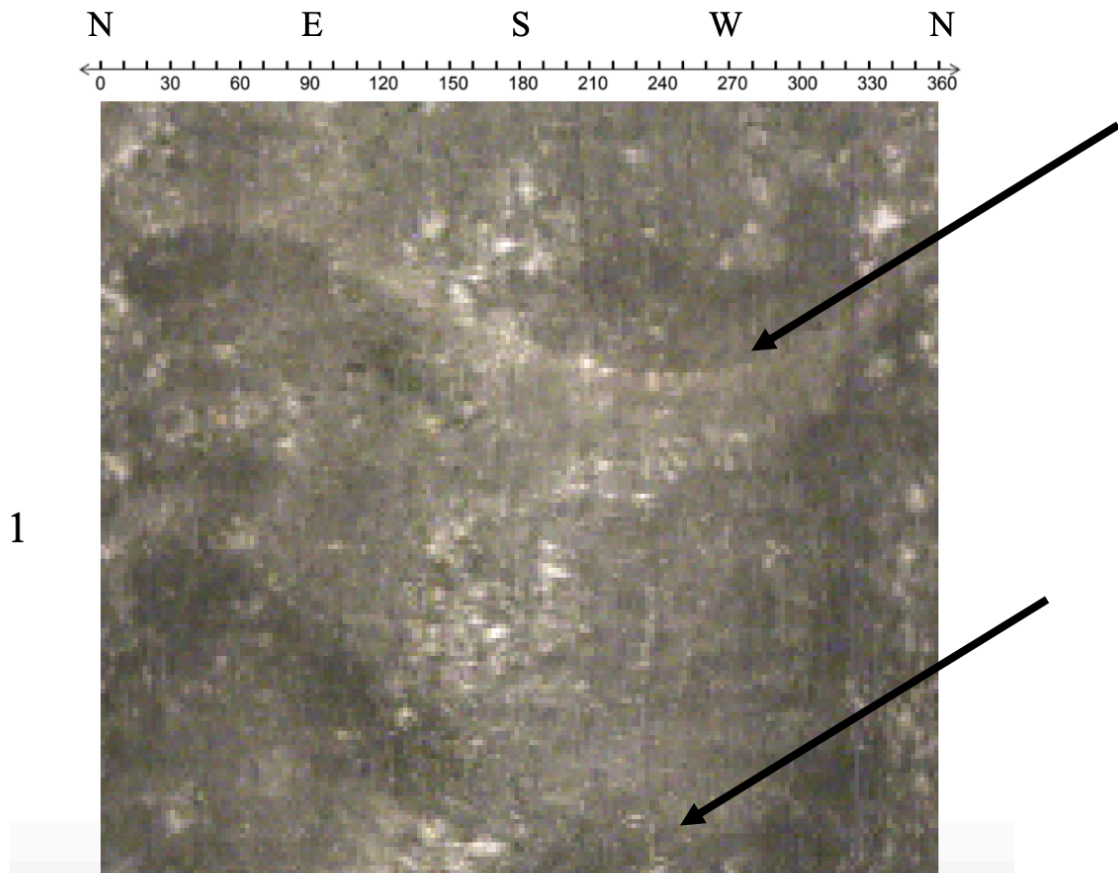


Figure 2

Example of “unwrapped” televiewer imagery with azimuth scale of angles 0-360° paired with North, South, East, and West included along the top. This segment is at approximately 1m depth in core JE. The two black arrows point to a light structure (top) representing a debris band, and a thicker darker structure (bottom), most likely a refrozen fracture.

Thin Sections

Ice thin sections for cores JA and JE were previously made by Stephanie Mills approximately every couple of meters through the full depth of the core. I made thin sections of core JB in the ice core freezer on the University of Maine campus. In the field, each ice core was divided into segments of about 0.5m length and labeled by segment number and core depths. Prior to cutting the ice, I measured the total length of the core segment and marked the side that represents the physical “up-direction” in the glacier in multiple places to ensure there were still visible markings if one rubbed off. Cores were cut with a handsaw to make an ice puck about 2-cm thick. Cutting the pucks as thin as possible allows less ice to be wasted when making the thin section, however, the handsaw did not provide enough precision to cut pucks thinner than 2-cm.

After cutting the pucks, the side pointing in the “up-direction” was clearly marked again, and the bottom of the puck was shaved as flat as possible using various grained sandpaper. The coarse sandpaper was sufficient for thinning the ice, but the finer sandpaper was necessary for polishing the surface, so as to produce a thin section with more visible features. Razor blades were the most effective to cleave the puck into an area that would fit on the 5.5x7.5cm glass slide. In order to adhere the ice to the glass slide, the ice was placed on the glass and I carefully dropped water around the edges, which froze within minutes. The ice puck must be as flat as possible to prevent water from seeping underneath during the gluing process, which makes it impossible to view any grains under cross-polarized light. Once the ice was successfully glued, razor blades and sand paper were used to shave the sample down to approximately 0.5mm thickness, or until grain boundaries were clearly visible.

After each sample was made it was placed between circular-cross-polarized lenses on a light table. The apparatus also included a mount for a camera and the ability to spin the lenses on either side of the sample, (Fig.3). As shown in Fig. 3, the outer part of the lens was marked at 0° , with lines marking subsequent angles that are multiples of 22.5° . The camera was mounted to take photographs with the crossed-polarized lenses at each 22.5° interval from 0° to 90° . Polarized light is a common technique in microscopy when studying polycrystalline substances, as the orientation of a grain's c-axis produces different birefringence colors. This is caused by the way light interacts with the crystalline structure of a material. Light waves are refracted into two different rays, between cross polars, and travel at different velocities, creating the colors in thin sections, (Fig.4). Cross-polarized lenses are necessary to distinguish each individual grain in the sample. I analyzed 14 thin sections from core JA and 6 from JE, and made and analyzed 8 from core JB, for a total of 28 thin sections.

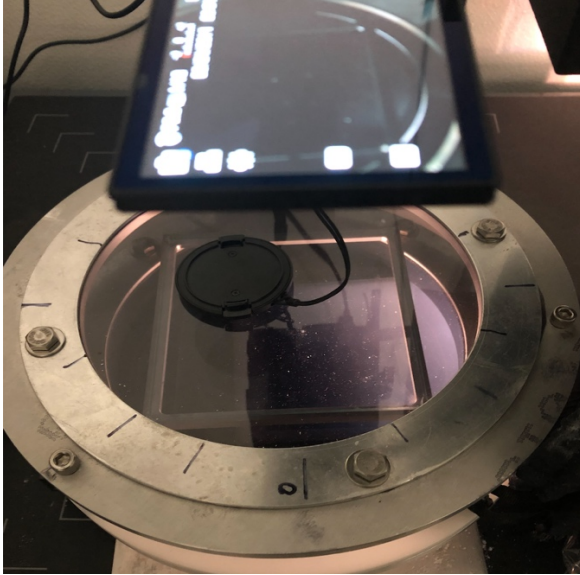


Figure 3

Photograph from the ice core freezer showing the cross polarized lenses which are inside of the metal rings, with light coming up through from the light table underneath. The metal ring is marked with evenly spaced lines and a “0” for reference, so the cross polars could be rotated at the same angle intervals. The square stand in the middle of the lenses is where the samples go. The camera screen is visible on the top.

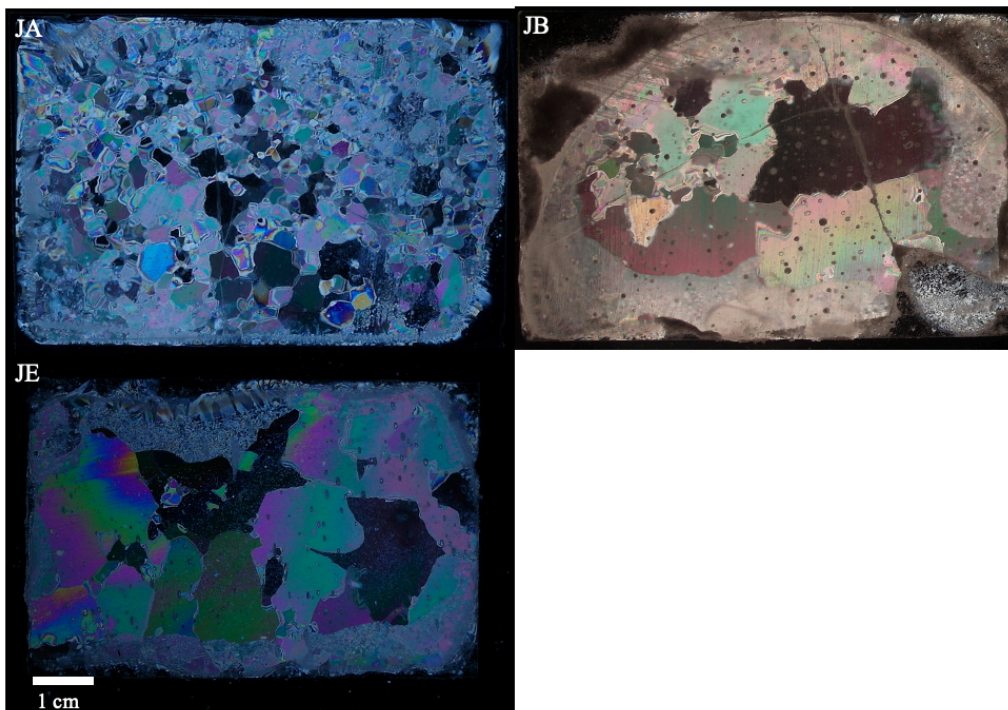


Figure 4

Thin section photos of JA35, JB32, and JE10 labelled by their respective core. The scale is represented by the white line which equals 1cm length.

Image Analysis

Photographs of the thin sections were uploaded onto the computer and one photo for each sample was chosen for analysis. I selected the photographs on the basis of which showed the most distinct grain boundaries. Some photographs, however, showed certain smaller grains better, so they were considered when outlining certain grains.

I used the imaging software, Adobe Illustrator, to delineate grain boundaries and bubbles (Fig. 5). Using the pen tool, grain boundaries were manually outlined with a series of line segments. The ellipse tool, in Illustrator, was used to outline the bubbles, with each one properly elongated and rotated. Every grain was outlined in every sample and at least 50 bubbles were analyzed for each sample. When a sample has less than 50 bubbles, a bubble analysis was not performed. On another layer in Illustrator, a line, extending the length of the long side of the glass slide, was made for future conversions from pixel units to metric units.

Adobe Illustrator files were converted to TIF file types to import into the image analysis program, ImageJ. In order to convert to millimeters later, the pre-programmed scale was removed prior to color thresholding. The line representing the glass slide length was measured for conversion. Then each image was color-thresholded multiple times, to eventually make black particles on a white background. ImageJ then provided measurements for various parameters through the “analyze particles” function. For measurements such as major/minor axis and aspect ratio, ImageJ determines a best fit ellipse for each particle using the same central point, size, and orientation.

Certain parameters measured by ImageJ, such as grain size, grain circularity, bubble aspect ratio and bubble angle or orientation, were selected for final analysis,

(Table 1). As mentioned, the glass slide length (75mm) was the conversion factor between pixels and millimeters which was squared for grain size calculations. Besides grain size, the remainder of the measurements emphasized in this analysis were unitless, so no conversions were required. For grain circularity, ImageJ uses the equation: $4\pi A/P^2$, where A=area and P=perimeter. To calculate bubble aspect ratio, it divides between the long by the short axis of each ellipse. A value of 1.0 for both aspect ratio and circularity indicates a perfect circle. Bubble angle is measured by taking the angle between the major axis of the particle and the X-axis of the entire image. These measurements are more concisely described in Table 1 below:

Image J Measurement	Calculation	Variable Definition	Units
Area (Grain Size)	Measures number of square-pixels	N/A	Pixels ² → mm ²
Circularity (Grains)	$4\pi A / P^2$	A = Area P = Perimeter	Unitless
Aspect Ratio (Bubbles)	Major axis / Minor Axis	Major Axis = Primary (long) axis of ellipse (bubble) Minor Axis = Secondary (short) axis of ellipse (bubble)	Unitless

Table 1

Measurements taken in ImageJ, the calculation performed in the program, definition of the variables used in calculation, and the units used for each measurement.

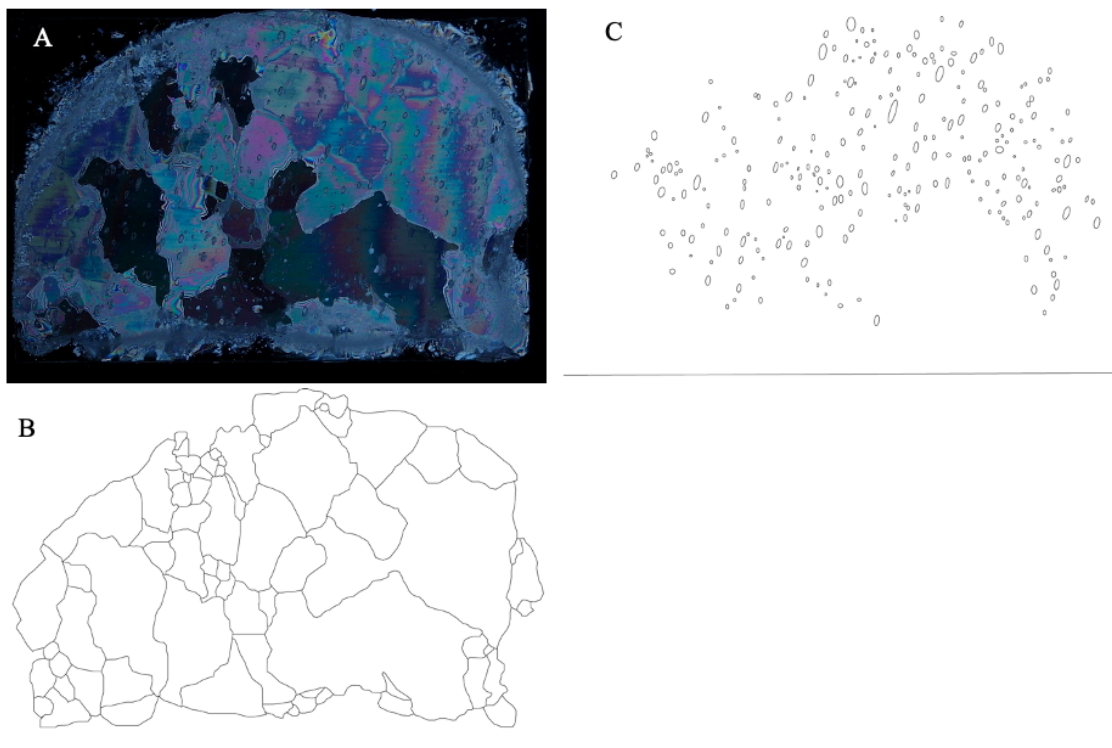


Figure 5

A: Image of thin section (sample: JE12) on a light table. Grain boundaries and bubbles are clearly visible. B: Grain boundaries of that sample delineated in Adobe Illustrator. C: Bubbles in that sample delineated and rotated in Adobe Illustrator. The black line at the bottom of the grain boundaries and bubble images is the line used to represent the glass slide, used to convert from pixels to millimeters.

Rose Diagrams

ImageJ prescribes an X and Y axis to each image and measures the orientation of particles by the angle between the long axis of the particle and the X-axis of the image. Bubble angles for each thin section were copied into a text file and then imported into Stereonet. For the purpose of this project, however, azimuth was not incorporated. When ice cores are extracted from boreholes, they are constantly rotating so determining the azimuth of the cores is nearly impossible. Other methods can be used to determine azimuth through feature matching in the ice cores and borehole imagery; but from experimentation during this study, errors have the potential to reach 45°. Unfortunately, due to this, the bubble orientations could not be compared between ice thin sections and could not indicate a cohesive direction of strain for each core. However, I was able to observe the alignment of bubbles within each thin section as well as perform interhole comparisons from representative samples.

In Stereonet, I created a rose diagram for each thin section. A rose diagram is a type of frequency plot where the “petal” length is dependent on the frequency of that orientation, or where it’s positioned on the circle. As mentioned previously, only one thin section could be plotted at once due to azimuth discrepancies between samples.

Statistical Plots

To begin data analysis, I exported all ImageJ measurements into Excel. Focusing on grain size, circularity, and bubble aspect ratio, I plotted an individual frequency histogram for each measurement for each thin section. Histograms were mainly used as they are fairly easy to read and clearly show distributions of datasets. For each core, I made a master histogram of all data from every thin section. Other histograms were made for representative samples, JA35, JB32, and JE10, which represent their respective cores. Line graphs were incorporated as well. Each line corresponds to an individual thin section, which was plotted with the same bins as the histograms and percentage frequency. These show how heterogeneous these properties are within a single core. The master and representative histograms were plotted with the number of grains or bubbles that populated each bin, however the spider plots used percentage to make it more easily comparable across thin sections.

An important aspect of studying the entire length of an ice core is to observe changes in the ice with depth. For the three cores, I calculated the means and standard deviations for every thin section and plotted them with depth obtained from the drill log. Standard deviations from the datasets were used as positive and negative error bars in the depth plot.

RESULTS

Televiewer Feature Orientation

Core-JA has a cluster of both bright and dark bands that dip northeast and a smaller cluster dipping southwest, but they are still spread out. Fewer structures exist in core-JE due to it being almost 60m shorter than JA. Minor clustering occurs in JE except for a small cluster dipping northeast. No structures in JE dip southwest. Both cores exhibit intermingled dark and bright bands.

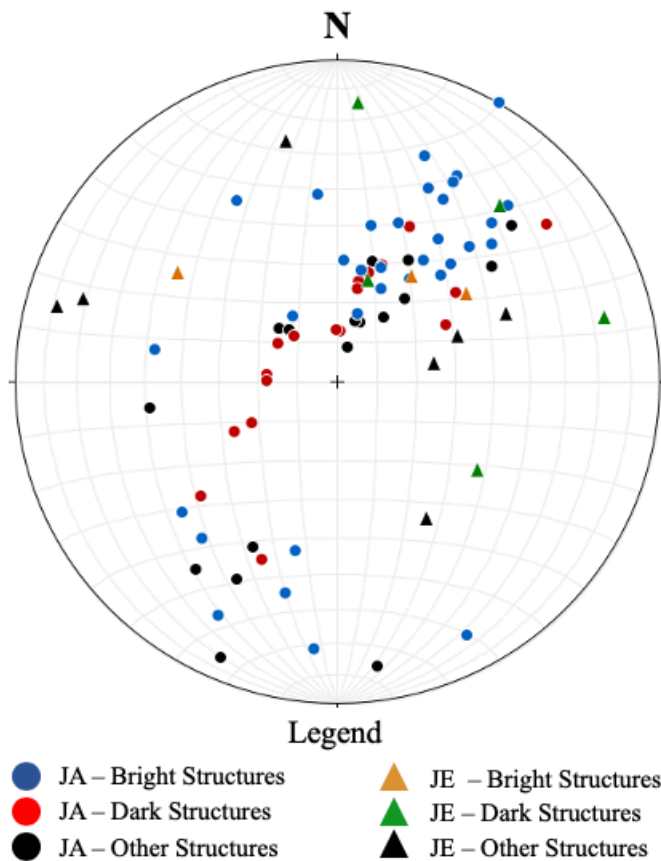


Figure 6

Stereographic projection, created in the program Stereonet, of dipping structures measured from borehole televiwer imagery in cores JA and JE. Circles show structures in JA, triangles in JE, and the colors are described in the legend above. The “N” indicates the North-direction of the graph.

Bubble Orientation

Representative samples for each of the three cores, JA35, JB32, and JE10 yield a total of 114 bubbles for JA35, 177 in JB32, and 107 in JE10. The rose diagram shows a bimodal distribution of bubble orientations for JA35 (Fig. 7). The two main peaks in this sample are approximately perpendicular to each other. The longest petal of nearly 30 bubbles occurs between 90° and 100° . Another, shorter petal represents about 15 bubbles between 80° and 90° . Another cluster of about 20 bubbles is oriented at 0° .

The rose diagram for JB32 represents a total of 177 bubbles, (Fig. 8). Similar to JA, there is a bimodal distribution of bubbles with the greatest number of bubbles in two petals centered around 0° . Almost 30 bubbles are oriented between 0° and 10° and about 25 bubbles between 350° and 360° , which is equivalent to 0° . A smaller cluster of bubble orientations occurs around 90° , with almost 20 bubbles between 80° and 90° and nearly 10 bubbles between 80° and 90° .

Sample JE10 has a rose diagram shows a consistent, unimodal distribution, (Fig. 9). The longest petal, of approximately 55 bubbles, are oriented between 90° and 100° . Between 80° and 90° there are nearly 100 bubbles.

Although representative samples were used in this analysis due to the inability to compare all the data in each core at the same time, cores JA and JB had consistent bimodal distributions and a unimodal distribution JE

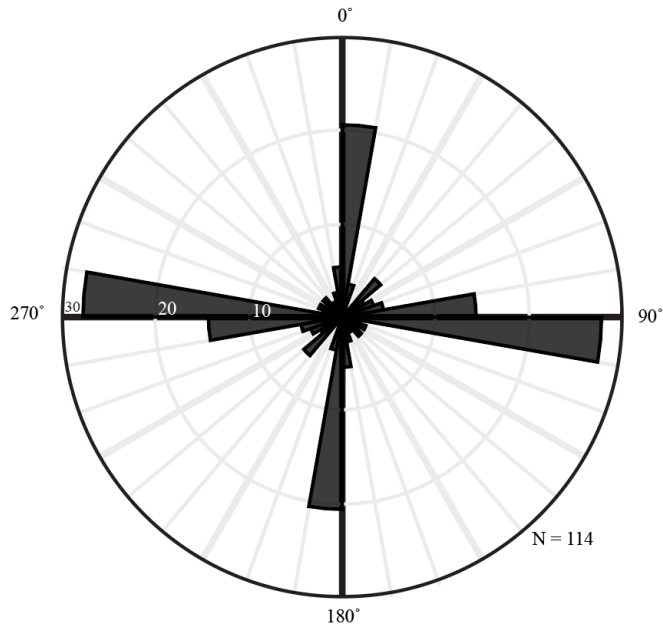


Figure 7

Rose diagram of bubble orientations for sample JA35, with a total of 114 bubbles ($N=114$). “Petal” length is determined by the number of bubbles with each light grey concentric circle representing intervals of 10.

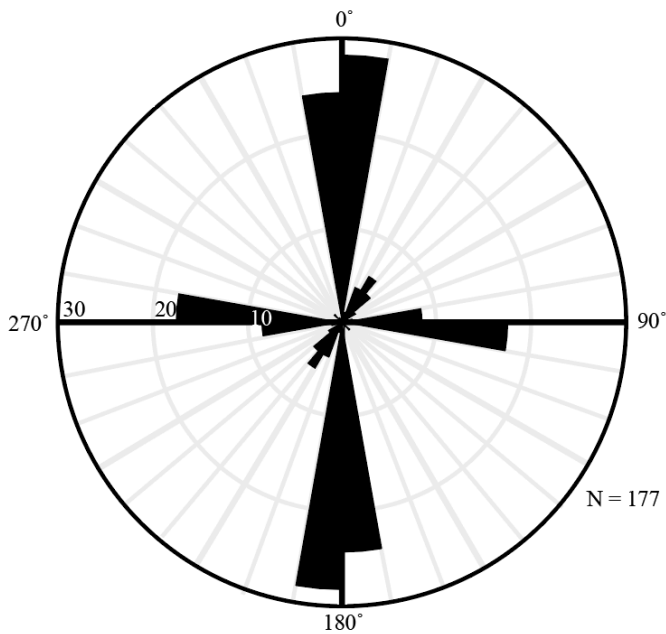


Figure 8

Rose diagram of bubble orientations for sample JB32, with a total of 177 bubbles ($N=177$). Petal length is determined by the number of bubbles with each light grey concentric circle representing intervals of 10.

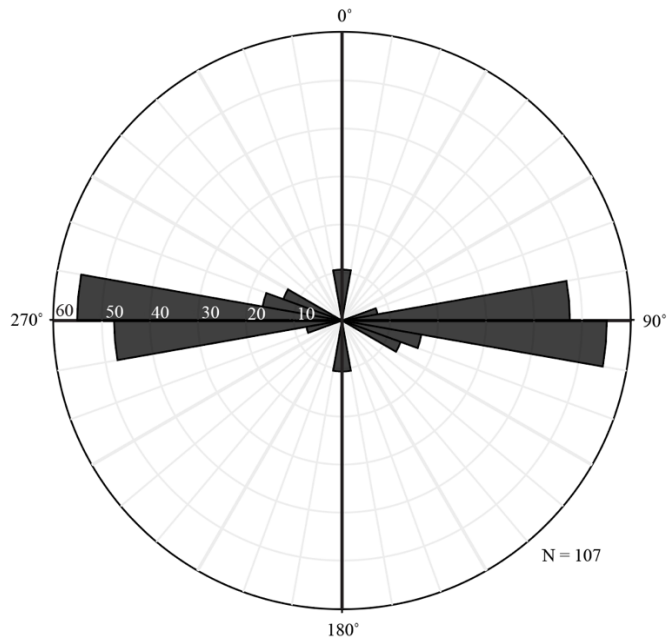


Figure 9

Rose diagram of bubble orientations for sample JE10, with a total of 107 bubbles (N=107). Petal length is determined by the number of bubbles with each light grey concentric circle representing intervals of 10.

Grain Size

Grain size data is represented by master histograms of each core, a representative histogram for each core, and line graphs for intracore comparisons. The total number of grains measured in cores JA, JB, and JE, is 5115, 2652, and 685. All three of the cores show right-skewed distributions with the majority of grains between 0.5 and 2.0mm² (Fig. 10). The overflow bin ($\geq 20\text{mm}^2$) for JA includes about 152 grains, or about 3% of the total grains. JB has 81 grains or 3% of the total grains. JE has 108 grains, 16% of all grains.

The samples, JA35, JB32, and JE10 are representative for each of the cores and were compared on the basis of grain size, grain orientation, and bubble shape and orientation (Fig. 11). For grain size, JA35 data are skewed right with the majority of grains between 0.5 and 2.0mm². JB32 also shows a right skew and the majority of grains in the same bin as JA35. The most populated bin in JE10, however, is the overflow bin which is composed of 14 grains, or 24% of the thin section. Overflow bin population for JA35 and JB32 are 2% and 11%, respectively.

The line graphs show the percentage of grains in each size bin, with each of the lines representing each of the thin sections in all three ice cores (Fig. 12,13,14). JA shows a right skewed distribution with most thin sections having the same peak. Approximately 50% of grains fall in the 0.5mm²-2.0mm² bin. The majority of thin sections are close to 0% for subsequent bins with the exception of the overflow ($>20\text{mm}^2$) bin. However, these percentages range from nearly 0% to approximately 55%. Thin sections in core JB show a spike at the 0.5-2.0mm² bin to approximately 45%, while the overflow bin ranges from nearly 0% to 100% across thin sections. The dot represents sample JB46-1a2, which

has a total of 5 grains, all them larger than 20mm^2 . Core JE peaks at both the underflow and overflow bins, but the thin sections are relatively uniform in between.

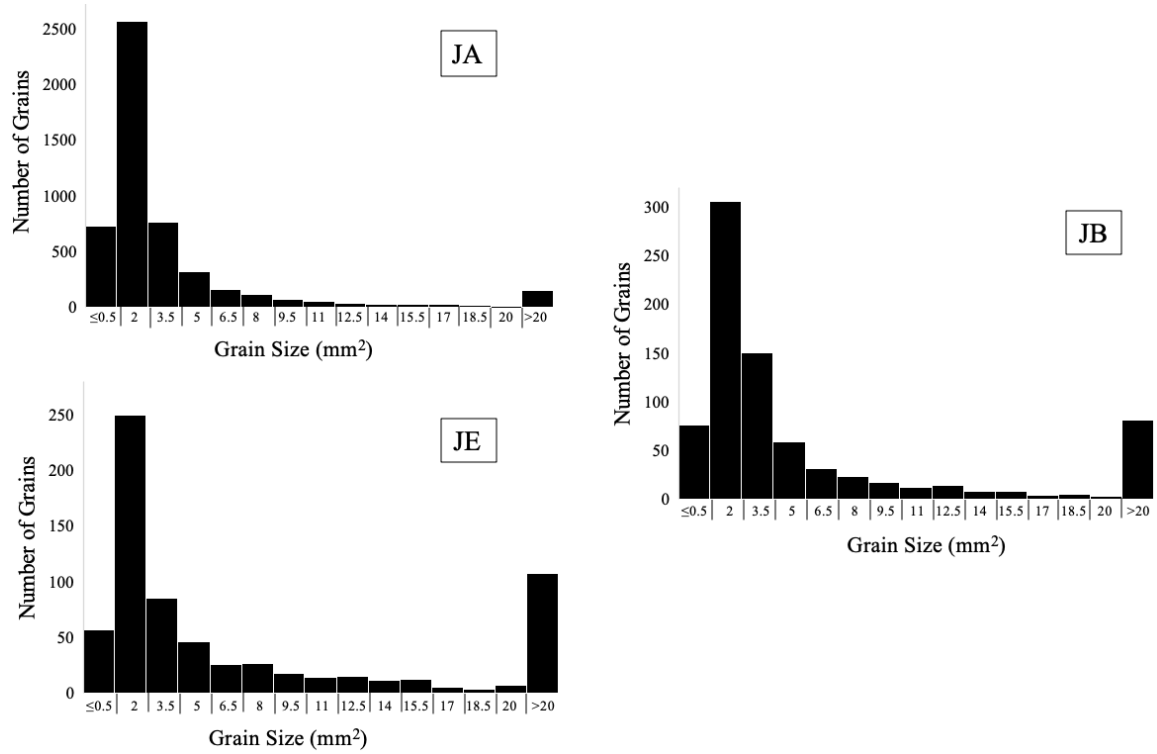


Figure 10

Histograms showing all grain size data from each core. The bin width for each core is 1.5 mm^2 with an underflow bin of $\leq 0.5\text{mm}^2$ and $>20\text{mm}^2$. The total amount of grains analyzed in cores JA, JB, and JE, are 5115, 2652, and 685, respectively. The x-axis indicates the upper bound for each bin, and the y-axis indicates the number of grains.

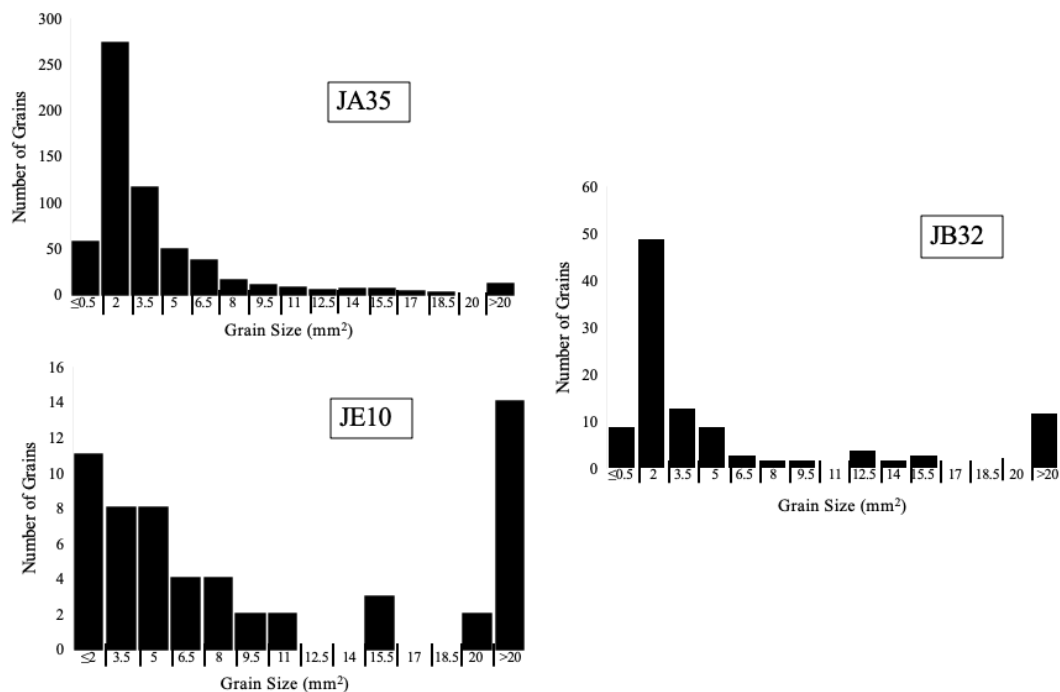


Figure 11

Grain size histograms for samples JA35, JB32, and JE10. Each histogram uses the same bin width of 0.1 mm² with underflow bins chosen at less than or equal to 0.5 mm², with the exception of JE10 due to the smallest grains being greater than 0.5 mm². The overflow bin for each histogram includes any grains larger than 20 mm². Each bin is labelled with the uppermost bound of the bin. The total amount of grains in each histogram, in the order JA, JB, and JE, is 591, 108, and 57.

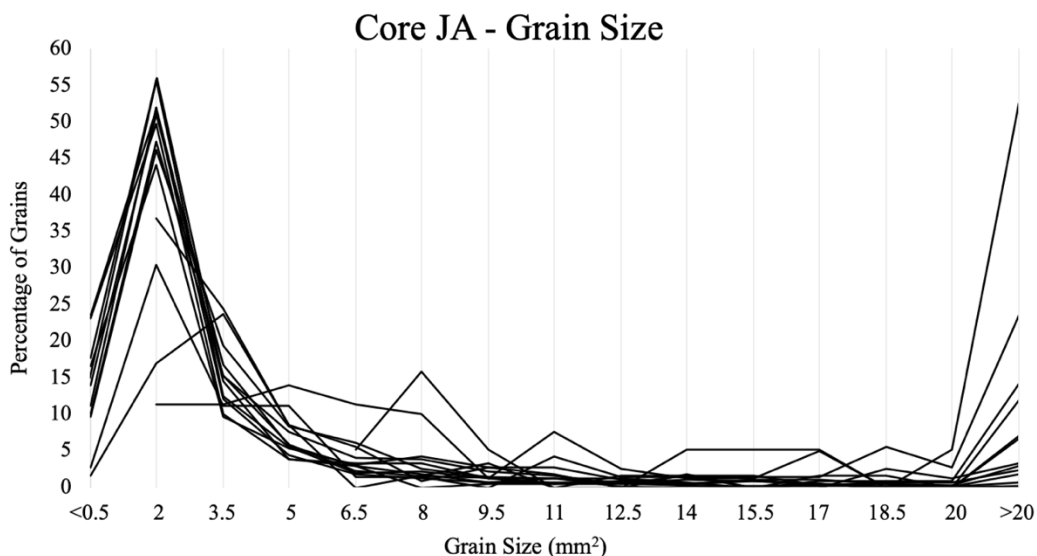


Figure 12

Line graph depicting all thin section grain size data for JA. Each line represents one thin section, with a total of 14 thin sections and 5115 grains. The x-axis numbers show the upper bounds of the bin. The y-axis marks the percentage of grains.

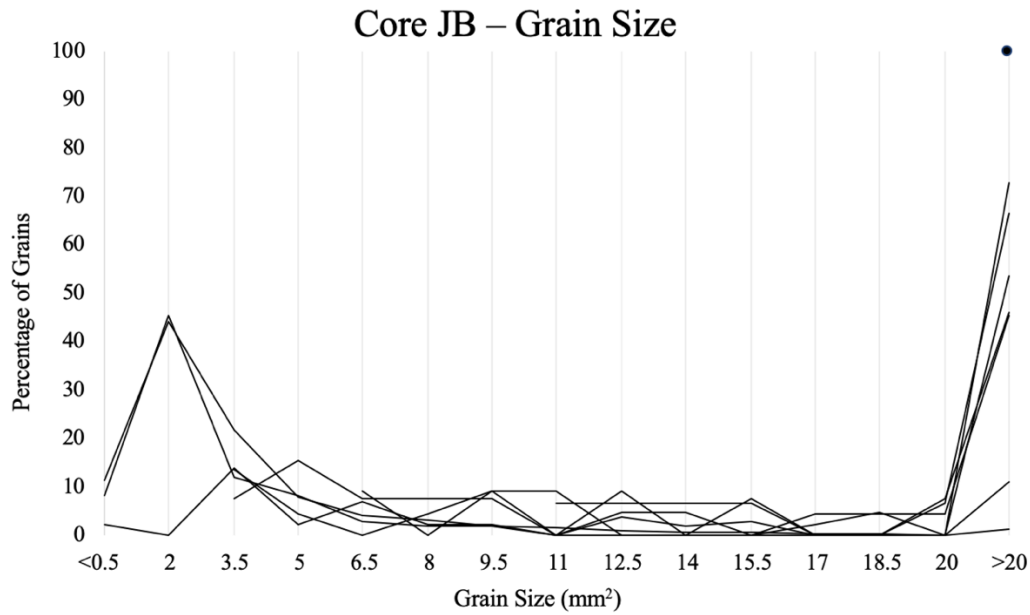


Figure 13

Line graph depicting all thin section grain size data for JB. Each line represents one thin section with a total of 8 thin sections and 2652 grains. The point labeled JB46a2 at 100%, shows that all of the grains were larger than 20mm^2 . The x-axis shows the upper bounds of bins and y-axis marks the percentage of grains.

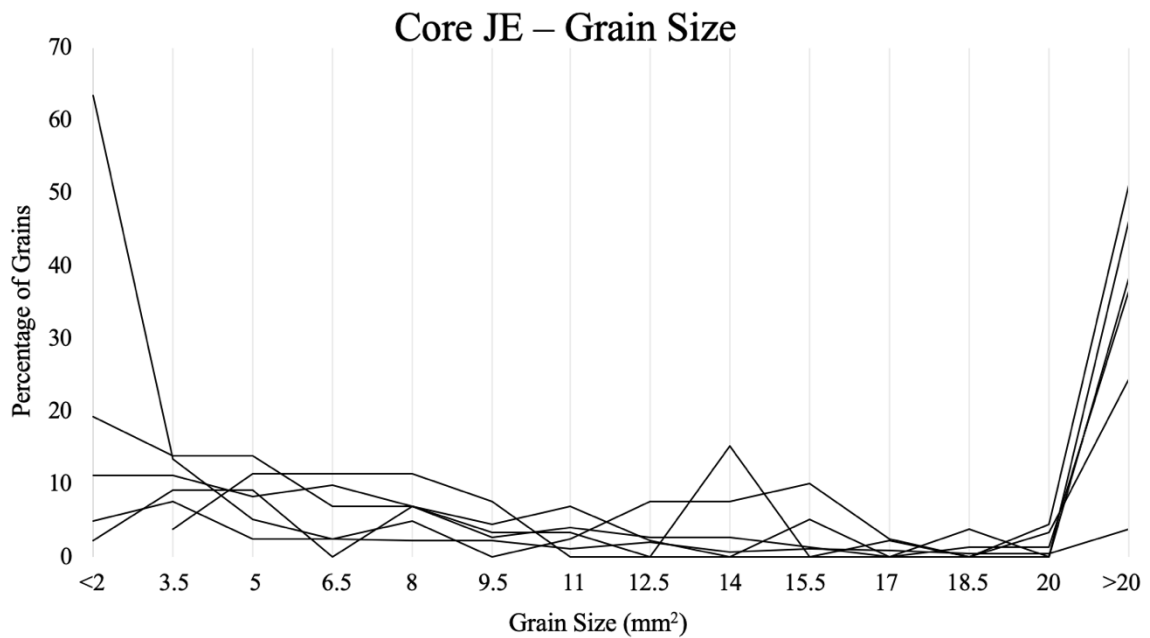


Figure 14

Line graph depicting all thin section grain size data for JE. Each line represents one thin section, with a total of 6 thin sections and 685 grains. The x-axis numbers show the upper bounds of each bin. The y-axis marks the percentage of grains.

Grain Circularity

Again, the total number of grains measured in each core is 5115 in JA, 2652 in JB, 685 in JE. The complete datasets for JA, JB, and JE show nearly normal distributions for all three cores (Fig. 15). JA shows a slight left skew along with JB. Both cores also are more concentrated in the 0.55-0.65 and 0.65-0.7 bins. Core JE has some grains distributed among the lower circularity values. For example, JE has 9% of grains with circularity value between 0.4 and 0.45 while JA and JB have 3.8% and 1.2%, respectively.

Histograms were plotted using JA35, JB32, and JE10 as representative samples, (Fig.16). The total number of grains in each histogram, in the order JA, JB, and JE, is 591, 108, and 57. Grain circularity is left-skewed in JA35 with the most populated bin being between 0.7 and 0.75, representing 20%. JB 32 is also left skewed with a uniform distribution among the lower-end circularity values. The highest number of grains, about 19% in JB32 have a circularity between 0.65 and 0.7. JE10 shows a bimodal distribution with clusters at 0.4 to 0.55 and 0.6 to 0.7.

The JA line graph shows an overall left skewed distribution with a peak of approximately 20% between 0.6 and 0.75 (Fig.17). Some of the thin sections, however, show a dip at those circularity values. According to its line graph, JB shows little cohesiveness between thin sections, (Fig.18). Some of JB's grain circularity data didn't fit within the prescribed bins due to values that weren't small or large enough. Core JE shows an overall spike at nearly 0.45 to 0.5 as well as at 0.65 to 0.75, though with little consistency between samples (Fig.19). Different degrees of variation occur among thin sections in all three cores.

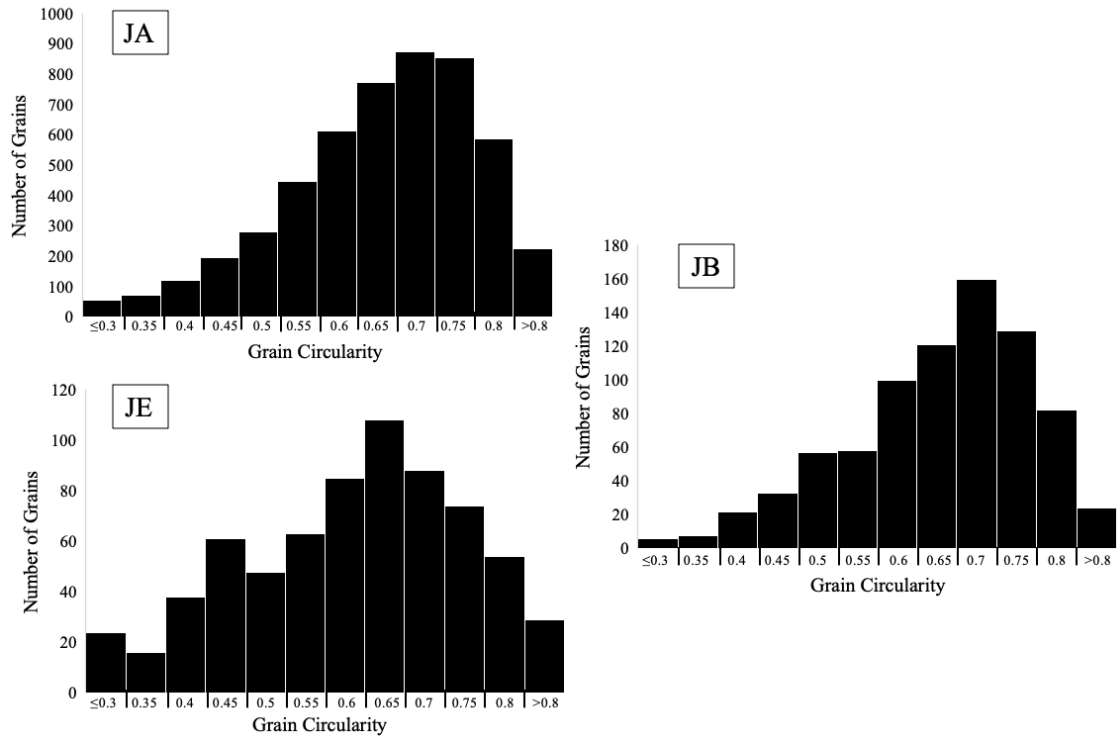


Figure 15

Histograms showing all grain circularity data from each core. The bin width for each core is 0.05 with an underflow bin of ≤ 0.3 and overflow bin of > 0.8 . The total amount of grains analyzed in cores JA, JB, and JE, are 5,115, 2652, and 685, respectively. The x-axis indicates the upper bound for each bin, and the y-axis is the number of grains.

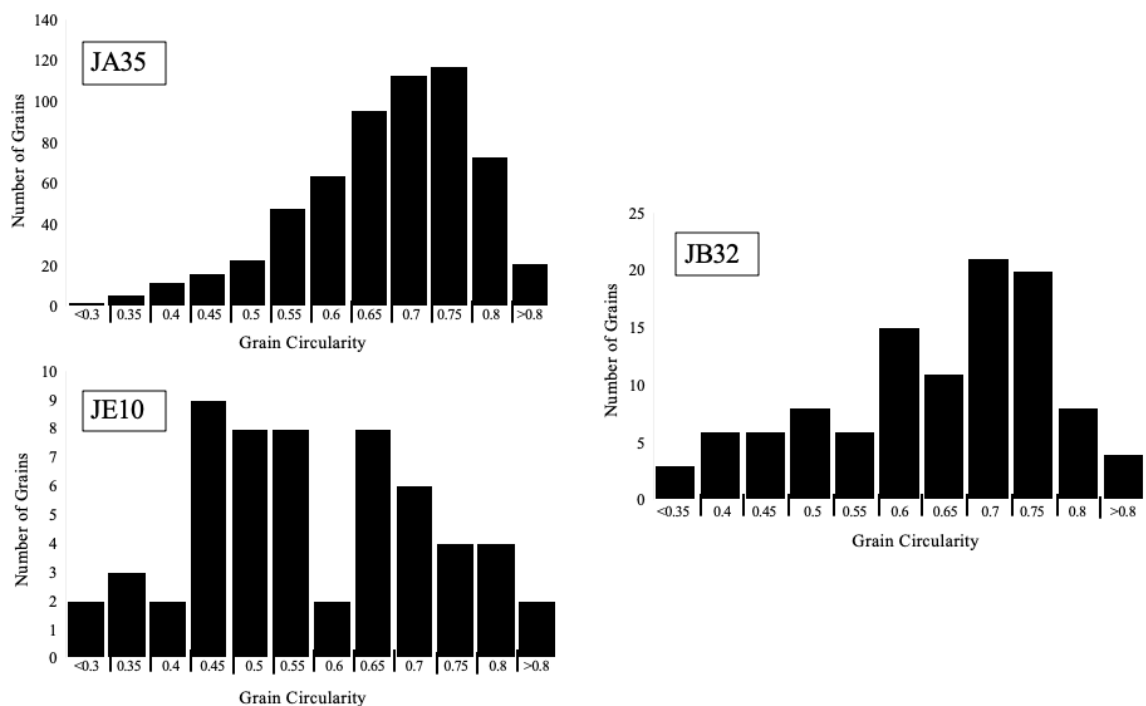


Figure 16

Histograms of grain circularity for samples JA35, JB32, and JE10. Each histogram uses the same bin width of 0.05 with an underflow bin of <0.3 in JA35 and JE10 and <0.35 in JB32. The overflow bin for each histogram includes circularity values >0.8. The x-axis is labelled with the uppermost bound of the bin. While the y-axis is the number of grains. The total amount of grains represented in each histogram, in the order JA, JB, and JE, is 591, 108, and 57.

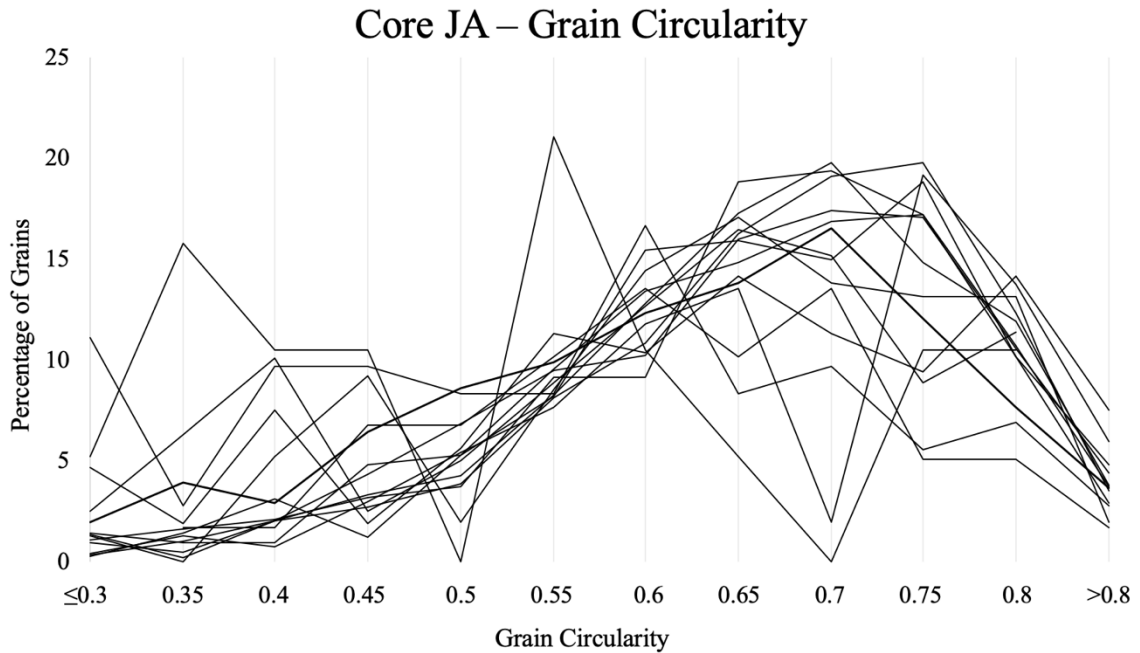


Figure 17

Line graph depicting grain circularity for JA. Each line represents one thin section, with a total of 14 thin sections and 5115 grains. The x-axis numbers show the upper bounds of each bin. The y-axis marks the percentage of grains.

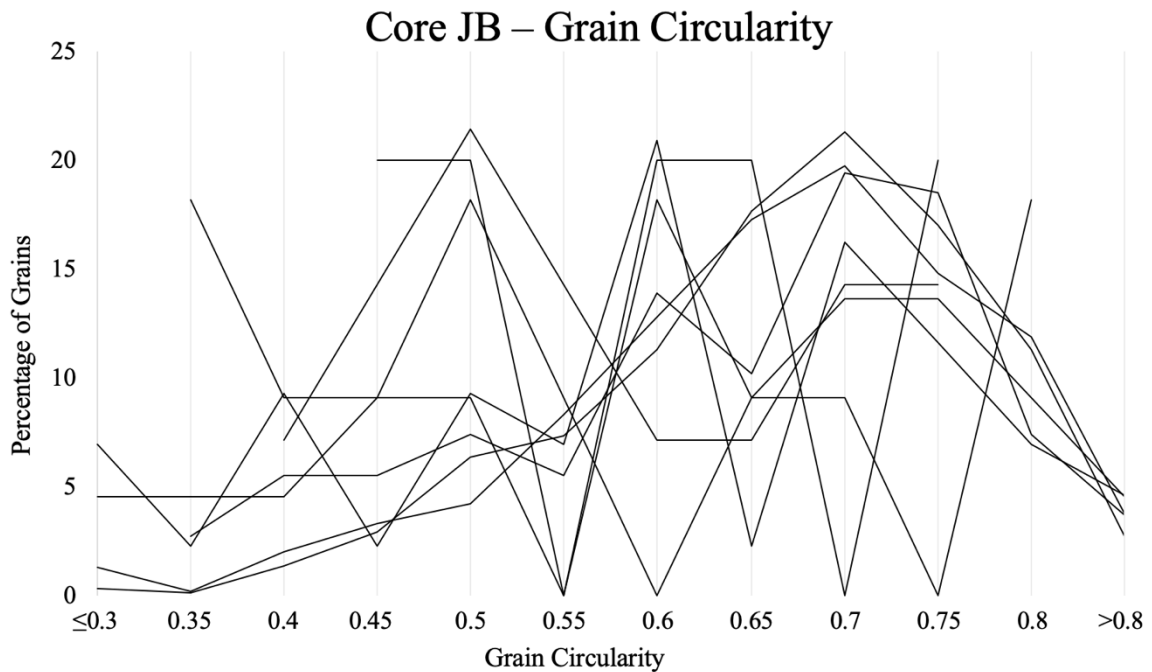


Figure 18

Line graph depicting grain circularity for core JB. Each line represents one thin section, for a total of 8 thin sections and 2652 grains. The x-axis shows the upper bound of each bin. The y-axis marks the percentage of grains.

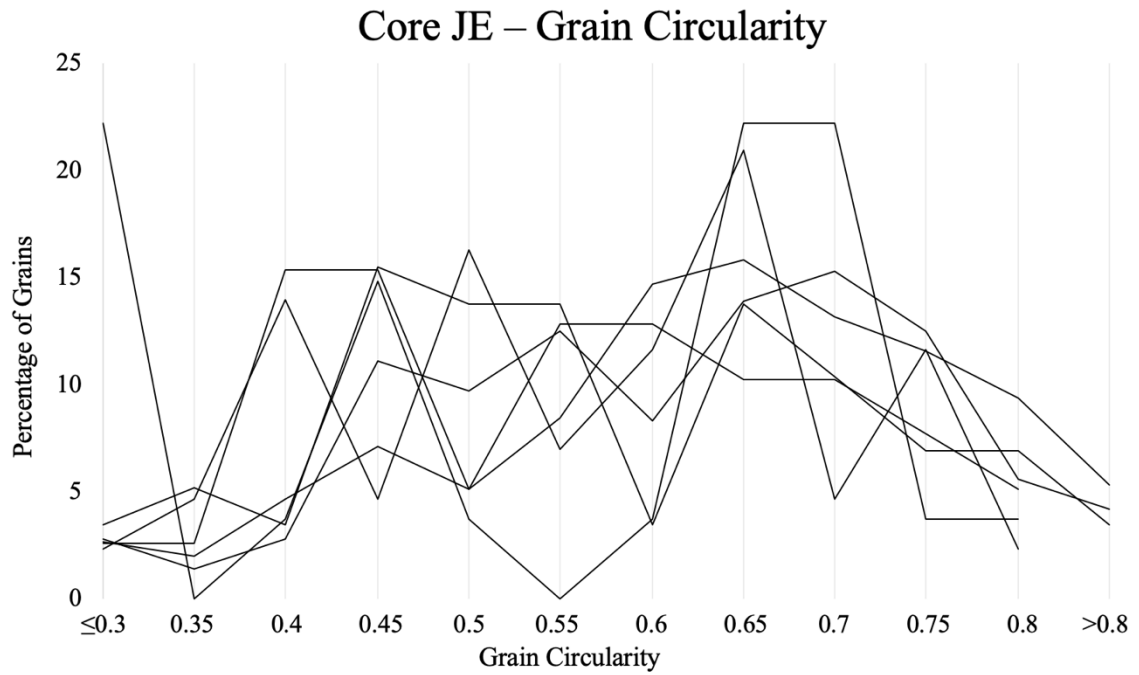


Figure 19

Line graph depicting grain circularity for JE. Each line represents one thin section, with a total of 6 thin sections and 685 grains. The x-axis numbers show the upper bounds of each bin. The y-axis marks the percentage of grains.

Bubble Shape (Aspect Ratio)

The master histograms for bubble aspect ratio data show that core JA is right-skewed with the majority, about 25% of the total amount of bubbles, in the 1.05-1.15 bin, (Fig.20). The overflow bin, any bubble with an aspect ratio greater than 2, has 67 bubbles, or 9% of the total. JB shows a right skew with the majority, about 28%, of bubbles having an aspect ratio between 1.05 and 1.15. The overflow bin, however, has 31 bubbles, or 1.6%. Core JE data is left-skewed. The majority, which is 204 bubbles accounting for 24% of all bubbles, have aspect ratios greater than 2.

JA35, JB32, and JE10, (Fig.21). JA35 is right skewed with about 27% of bubbles falling between 1.05 and 1.15 aspect ratios. There was only one bubble measured greater than 2. Similarly, JB32 data is right-skewed with 28% of aspect ratios between 1.05 and 1.15, and only 2 bubbles with aspect ratios greater than 2. JE10 distribution is left-skewed with 34.5% of bubbles having aspect ratios greater than 2.

The spider plot for core JA bubble aspect ratio shows correlation between the thin sections with a peak occurring in all thin sections between 1.05 and 1.15, (Fig.22). The bubble percentage continuously drops as aspect ratio increases with a slight increase at the >2 bin. JB data is right skewed with a peak occurring at the same 1.05-1.15 bin, (Fig.23). Only one thin section shows a significant increase for the overflow bin. Core JE shows a peak at >2 for nearly all thin sections, (Fig.24). Less than 2.0, thin sections show a fairly uniform distribution of low percentages.

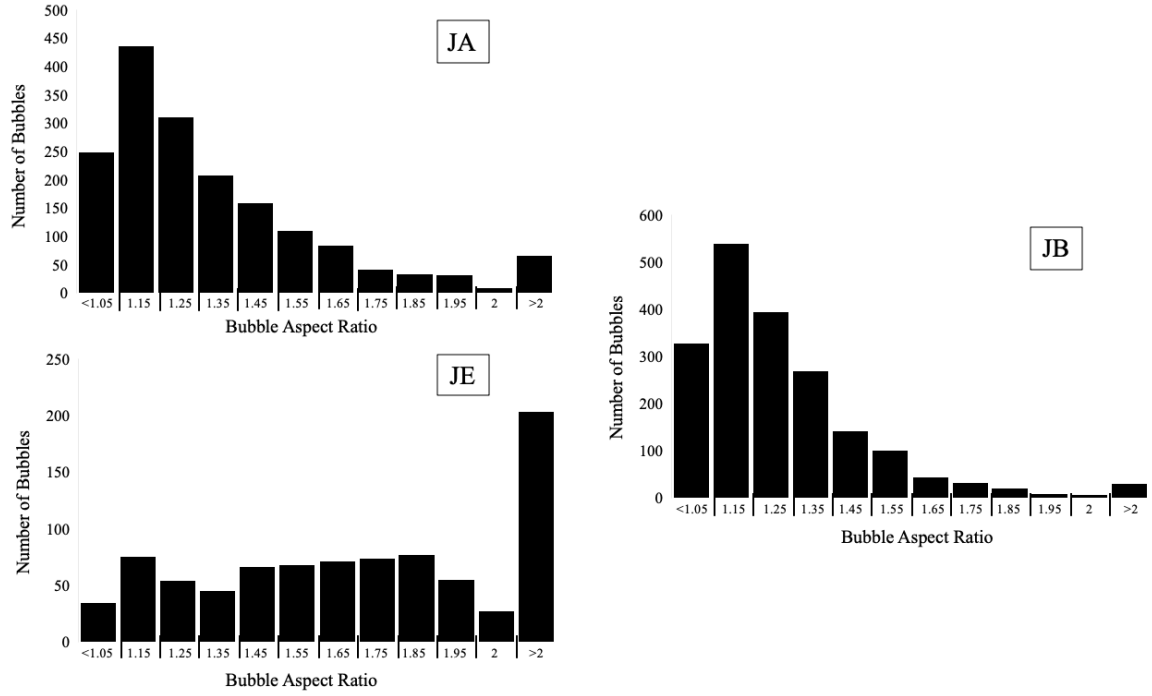


Figure 20

Histograms showing all bubble aspect ratio data from each core. The bin width for each core is 0.1 with an underflow bin of ≤ 1.05 and overflow bin of > 2.0 . The total amount of bubbles analyzed in cores JA, JB, and JE, are 1752, 1931, and 860, respectively. The x-axis indicates the upper bound for each bin, and the y-axis is the number of bubbles.

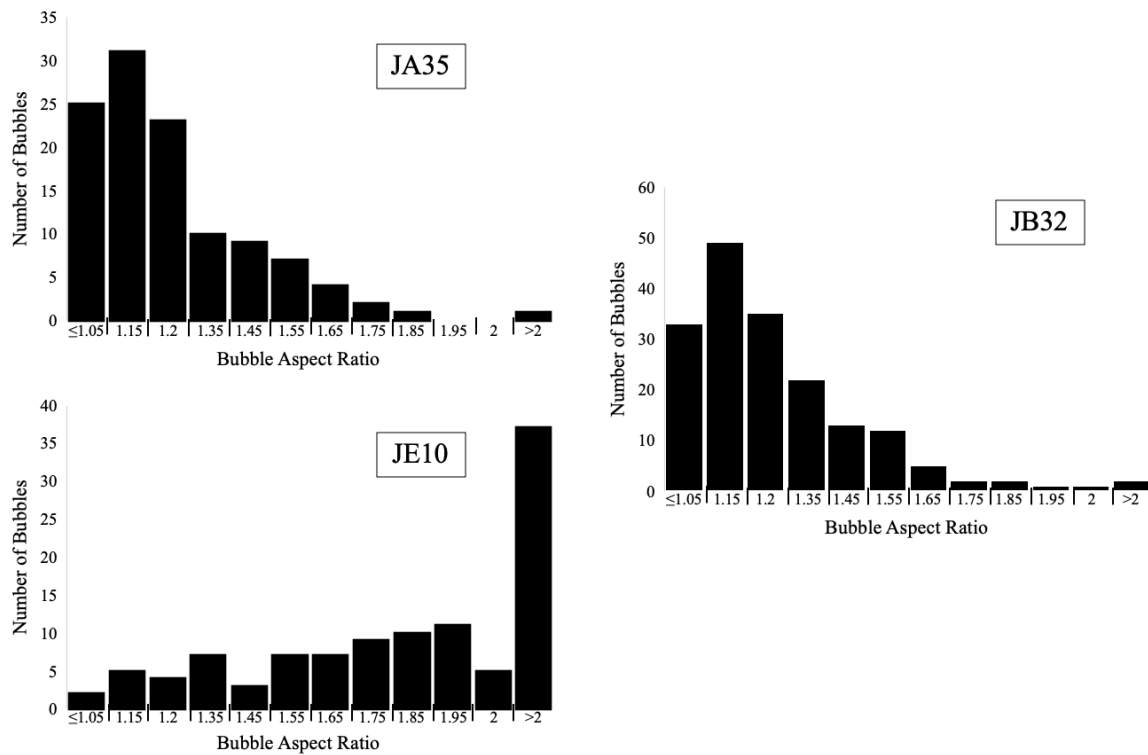


Figure 21

Histograms of bubble aspect ratios for samples JA35, JB32, and JE10, that are representative of their respective core. Each histogram uses the same bin width of 0.1 with an underflow bin of ≤ 1.05 and overflow bin of > 2.0 . The x-axis is labelled with the uppermost bound of the bin. While the y-axis is the number of grains. The total amount of bubbles represented in each histogram, in the order JA, JB, and JE, is 114, 177, and 107.

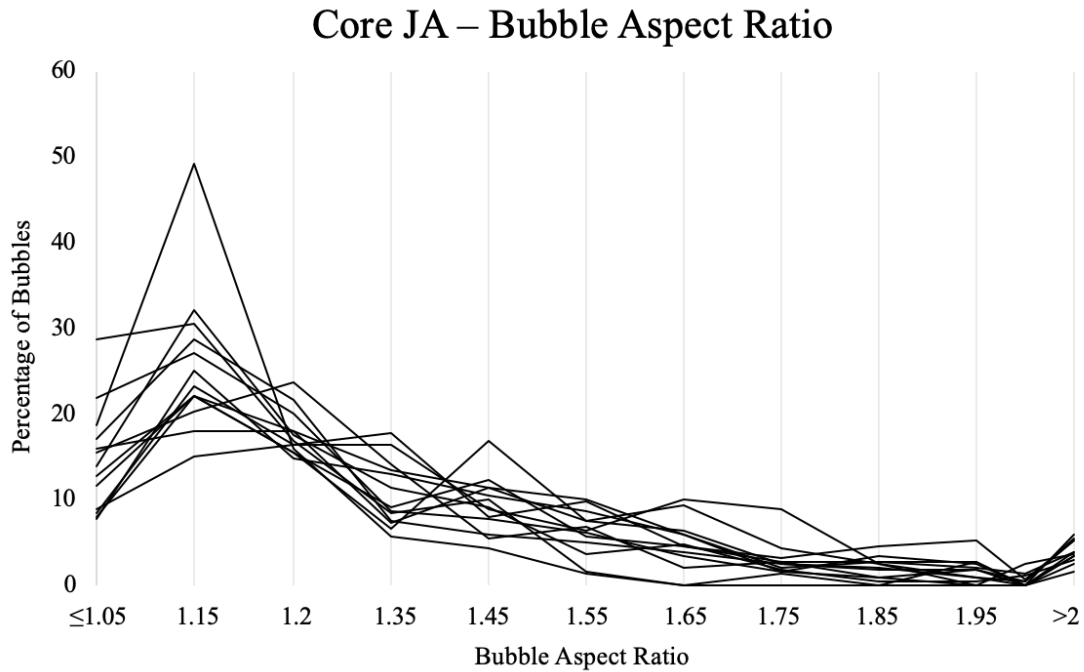


Figure 22

Line graph depicting bubble aspect ratios for JA. Each line represents one thin section, with a total of 13 thin sections and 1,844 bubbles. The x-axis numbers show the upper bounds of each bin while the y-axis shows the percentage of bubbles.

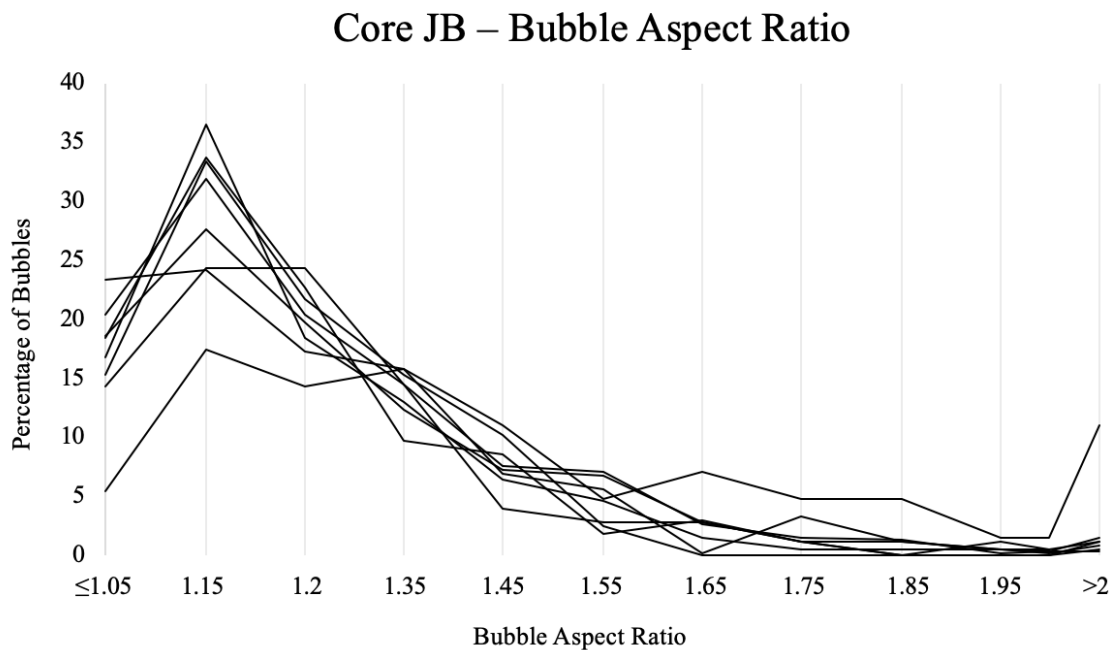


Figure 23

Line graph depicting bubble aspect ratios for JB. Each line represents one thin section, with a total of 8 thin sections and 1,371 bubbles. The x-axis numbers show the upper bounds of each bin while the y-axis shows the percentage of bubbles.

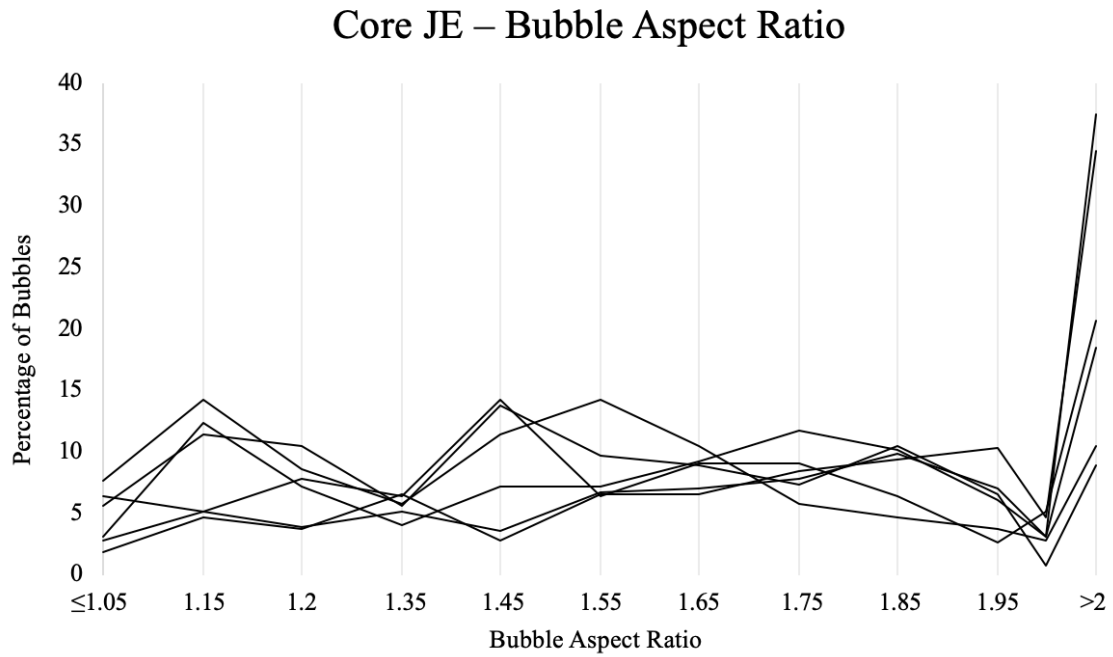


Figure 24

Line graph depicting bubble aspect ratios for JE. Each line represents one thin section, with a total of 6 thin sections and 860 bubbles. The x-axis numbers show the upper bounds of each bin while the y-axis shows the percentage of bubbles.

DISCUSSION

Intrahole Heterogeneity

Although horizontal strain rate gradients are a focus of this project and others when studying glacier flow, the heterogeneity within a single core must also be examined. Because grain size, circularity, bubble aspect ratio, and the orientation and angle of dipping bands are affected by strain, differences between thin sections may show vertical gradients in mechanics.

The line graphs provide a visual to compare the degree of variation between thin sections in a single core. Line plots for grain size (Fig.12,13,14) indicate that this metric was fairly cohesive within a core. Most JA samples have a similar grain size distribution, with a peak in grains between 0.5 and 2.0mm², though some samples have a greater number of grains larger than 20mm². JB and JE grain size spider plots indicate more variation between thin sections. Only two JB-samples peaked between 0.5 and 2.0mm². The remainder showed a higher percentage of grains greater than 20mm², with one sample having 100% of grains >20mm². Core JE showed more variation between samples than JA and JB, with the majority of grains either smaller than 2mm² or greater than 20mm². Heterogeneity of grain size between samples within a core may indicate mechanical differences occur with depth, or that different processes dominate at that scale.

Compared to grain size, grain circularity data shows a significant amount of intrahole heterogeneity. The core JA spider plot of grain circularity (Fig.17) shows a pattern of increasing circularity value peaking near 0.65 and 0.7. Other samples show much greater variation. Spider plots for cores JB and JE (Fig.18,19) show no cohesive

pattern between thin sections, although there are a couple of thin sections in JB that follow the same pattern.

Bubble aspect ratio spider plots show consistency between thin sections in all three cores (Fig.22,23,24). Core JA has little variation with a clear peak in aspect ratios between 1.05 and 1.15 decreasing as aspect ratio increases (Fig.22). JB also shows small variations between thin sections (Fig.23). Samples in JE differ more from each other, but the same pattern persists, with uniformly low percentages throughout the bins, until peaking at >2 (Fig.24). Rose diagram data from all of the samples show similar distributions in bubble orientation within cores. JA and JB are consistently bimodal, while JE is unimodal.

For further analysis of the relation between grain size, circularity, and bubble shape, the mean value of all of these measurements for each thin section was calculated and plotted with depth. JA grain size shows consistent average values that don't fluctuate significantly with depth, with the exception of the deepest sample (JA117) which is much larger (Fig.25). This is consistent with larger grains occurring deeper in the ice due to having more time to grow. However, JA117 also has the largest error bars due to a standard deviation of 152.6mm^2 . Throughout the rest of the core, error bars remain fairly uniform, with an average standard deviation of 26.5. JA grain circularity shows much more variation throughout the core than grain size, with an average standard deviation of 0.13 (Fig.26). Bubble aspect ratios show little variation for core JA with depth (Fig.27). Overall, JA shows a small amount of intrahole heterogeneity for grain size and bubble aspect ratio, but more for grain circularity.

Core JB shows little consistency among grain size averages when plotted with depth (Fig.25). The error bar lengths are also not consistent and range from 5.6 to 398.4mm². The line graph (Fig.18) suggests more consistency exists between thin sections in JB than the averages do. This indicates that in this case, means are not ideal for determining heterogeneity. Mean grain circularity data show some correlation with depth for JB, but error bars are large enough that the variations may be insignificant (Fig.26). However, the line plot shows heterogeneity within the core. Average bubble shape in JB doesn't possess much heterogeneity with depth, with the exception of the first thin section, (Fig.27). The first sample, JB23, has a mean bubble aspect ratio of 1.47 with a standard deviation of 0.46, which are both greater than the other values. Intrahole heterogeneity is greater in core JB. There are inconsistencies between the line graphs and the depth plots which may indicate that taking averages and analyzing their error bars is not ideal for making conclusions about heterogeneity, especially within a single core.

Core JE grain size averages are also plotted with depth, (Fig.25). There is some variation between means, but they remain relatively constant. Error bars, however, range in length from 44 to 140, showing that the uncertainty lacks uniformity. The grain circularity depth plot for JE indicates that there is some consistency between means and standard deviations, (Fig.26). The spider plot shows zero correlation between thin sections, again indicating that caution should be invoked when plotting mean values. Average bubble aspect ratio data for core JE range from 1.52 to 1.88, (Fig. 27). Plotted with depth there is some heterogeneity evident, however the error bars remain constant. Overall, there is heterogeneity within core JE, evident in grain size error bars and grain circularity. Bubble aspect ratio is fairly consistent, however.

Larger scale dipping structures also show how strain may differ vertically in a core. Examining both cores separately in the stereonet plot of bright and dark structures shows that all feature types are intermingled for both cores, (Fig.6). This indicates that the debris bands and refrozen cracks formed with the same family of orientations in each core, suggesting less intrahole heterogeneity.

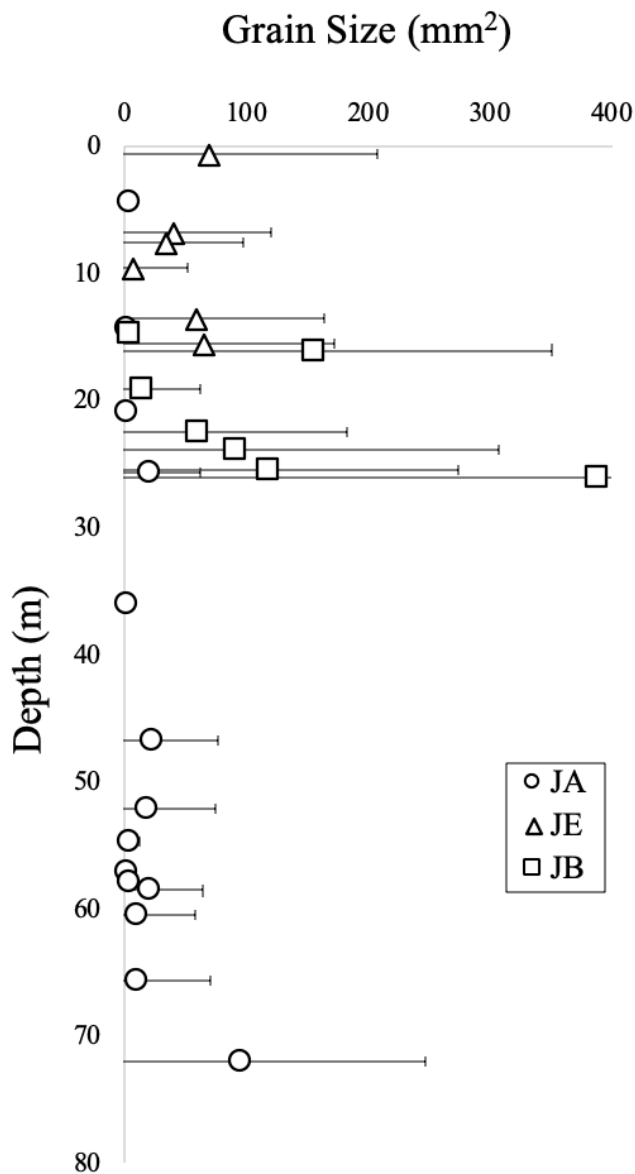


Figure 25

Mean grain size plotted with depth. Each marker represents one thin section. JA=circles, JB=squares, JE=triangles. Error bars are calculated from the standard deviation of each thin section dataset.

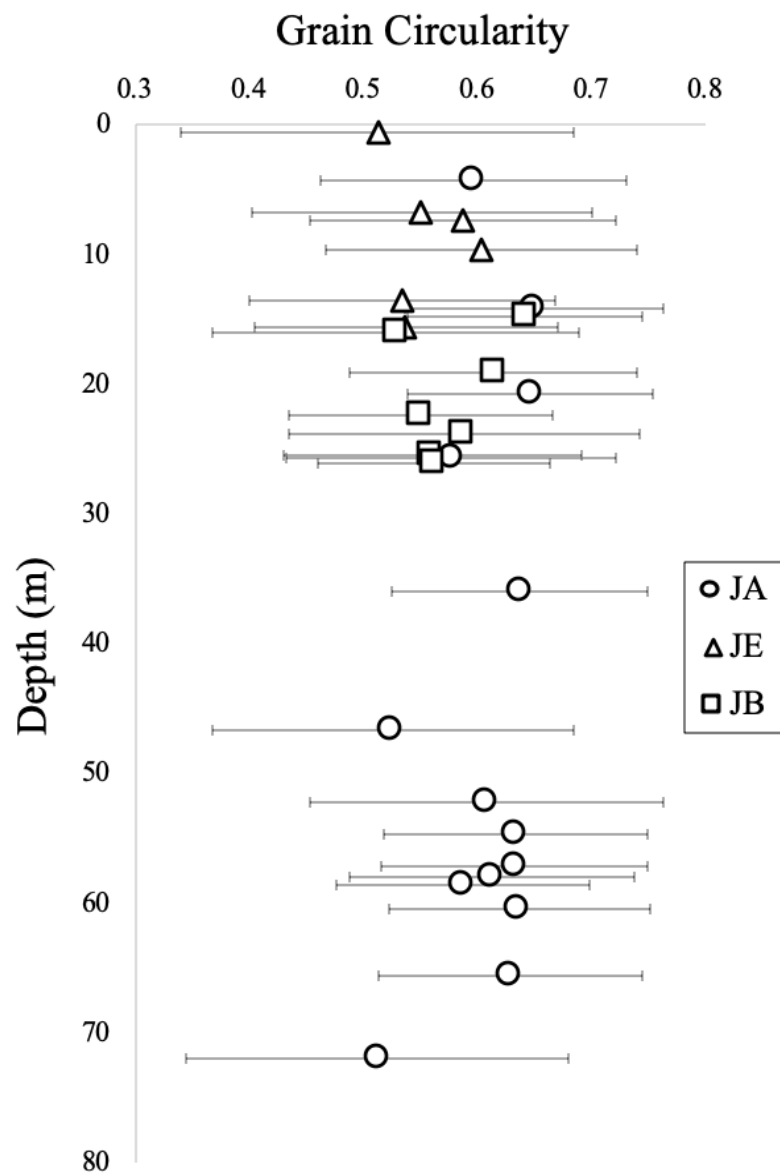


Figure 26

Mean grain circularity plotted with depth. Each marker represents one thin section. JA = circles, JB = squares, JE = triangles. Error bars are calculated from the standard deviation of each thin section dataset.

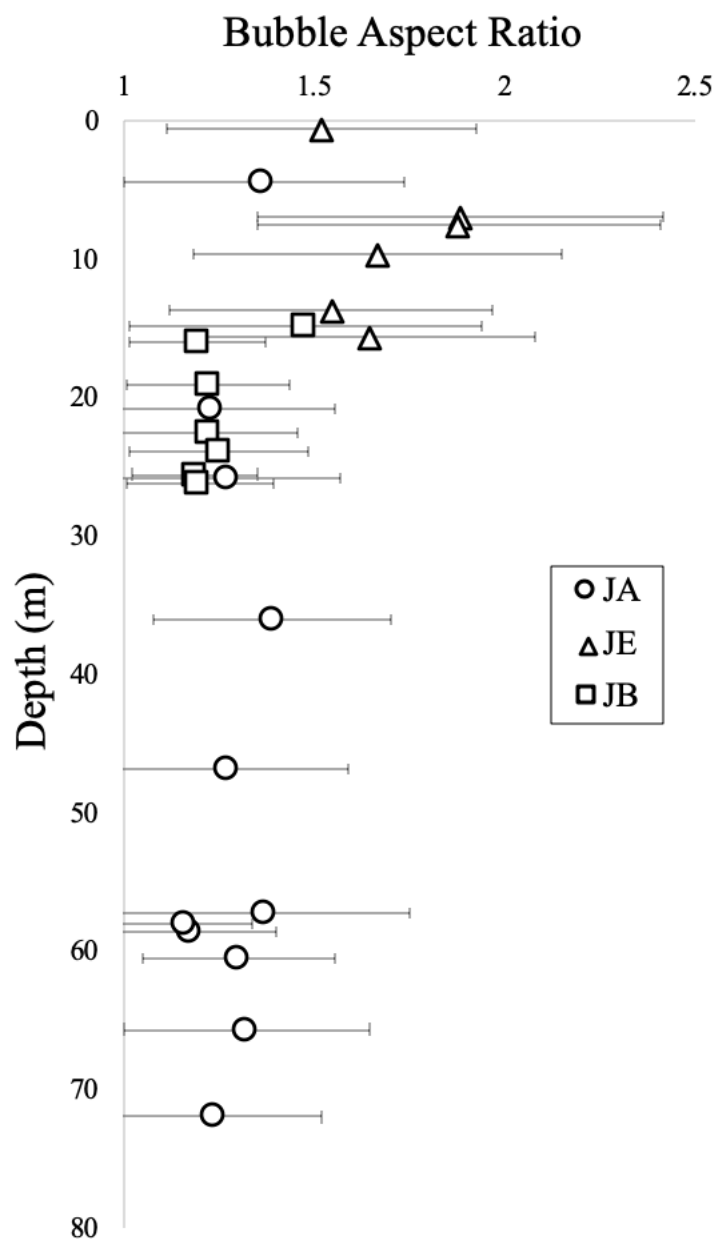


Figure 27

Mean bubble aspect ratio plotted with depth. Each marker represents one thin section. JA = circles, JB = squares, JE = triangles. Error bars are calculated from the standard deviation of each thin section dataset.

Interhole Heterogeneity

The datasets that include every grain size throughout an entire core show fairly similar distributions between the three cores. All of the master histograms are right-skewed. However, the number and percentage of grains in the overflow bin ($>20\text{mm}^2$) is greatest in core JE. About 3% of all grains fell in the overflow bin for cores JA and JB, but 18% of JE grains did. Although the histograms show similar distributions between JA and JB, the line graphs for JA, JB, and JE exhibit different behavior between the cores. For instance, although a similar pattern exists between JA and JB the spider plot shows that only two of the thin sections in JB peak at that grain size, (Fig. 13). One of the thin sections dips at that point, while the other three samples had grain sizes all well above 2.0mm^2 . The variation in JA grain size is also significantly less, as JB has small grains and also one with 100% of grains $>20\text{mm}^2$. JE shows greater variation than the other cores as well as different distributions from JA and JB

In the mean grain size plot with depth including all three cores, JA and JE show the strongest relationship. JE has larger grains on average, than JA, but they do not vary significantly and their standard deviations are relatively similar. In this graph, JB has the largest grains as well as the largest error bars and does not relate to JA and JE.

Grain circularity data in the master histograms is fairly similar across cores, with left-skewed data in JA and JB and a semi-normal distribution for JE. The spider plots, however, show significant differences between intracore heterogeneity. JA shows less heterogeneity throughout the core than JB and JE do. The average grain circularity plot (Fig.26) doesn't show significant variation between the three cores. Error bars are fairly consistent and the circularity values range between 0.51 and 0.65 for all of the samples.

Despite similar grain circularity values, JE shows the lowest average grain circularity values with JB next, and JA, the highest.

Aspect ratio data provided clear differences between JA/JB and JE. In all of the histograms JE had the majority of bubbles with aspect ratios >2 , while JA and JB were the opposite with right skewed data and small aspect ratios. This is also evident through observations of the thin section images themselves, (Fig.4). JE10 exhibits elongated bubbles, and the other two thin sections do not. The line graphs, (Fig.22, 23, 24), which show intrahole correlation in all three cores, have the same relationship as the histograms. Furthermore, this validates using the mean aspect ratio plot, (Fig.27), in interhole comparisons. Cores JA and JB are strongly correlated and have small aspect ratios between 1.0 and 1.5. JE, however, has values that range from 1.52 to 1.88, with these likely being a low representation due to a small number of more circular bubbles factoring into the mean.

Bubble orientation data cannot be compared within a single core, due to error between the thin section orientations themselves, so the representative samples (JA35, JB32, and JE10) are used for interhole heterogeneity observations. JA35 and JB32 bubble orientation data both show bimodal distributions centered around 0° and 90° , (Fig.7,8). JB shows less evenly divided modes, however. Using bubble orientation as a strain direction marker, this shows that JA and JB show less cohesive strain. JE10 has a unimodal distribution of bubble orientations with the majority pointing in the 90° direction, (Fig.9). This shows that JE has the most consistent orientation for bubbles and that heterogeneity exists for bubble orientation between cores, implying different directions of strain. Pairing this data with bubble elongation data may indicate how strain magnitude may

vary between cores. JE, for example, had the most elongate bubbles and uniform bubble orientation data indicating that at core JE there is either the greatest strain or a significantly dominant strain direction compared to the other two core locations.

Macroscopic structures exhibit different behavior in cores JA and JE, (Fig.6). The televiewer data shows light and dark structures. The colors, however, correspond to the opposite in the ice core photos taken on a light table. This is due to the position of the light which pointed in the same direction as the camera when the boreholes were imaged. For example, the lighter colored bands in the televiewer correlate to darker sediment bands in the core photos. The dark televiewer bands indicate where there is clear ice, lacking bubbles, showing up lighter in the core photos. These are most likely small fractures that have been refrozen. Fig. 6 shows that core JA has a cluster of structures that dip northeast, with some also dipping southwest. JE, however, has no structures that dip southwest, but a small cluster dipping northeast. Different dip directions in the two cores suggest that the kinematics differ closer to the lateral margin compared to closer to the center of flow. For a better visual, the circles and triangles were removed from the stereonet plot and the overall shape of the data distribution was traced in Adobe Illustrator, (Fig.28). The blue, representing JA, shows a different orientation and shape than the pink, or JE.

Overall, JA and JB show similar grain size, grain circularity, bubble aspect ratio, and bubble orientation data. They differ significantly from JE through histograms, stereonet graphs, and overall intrahole correlations. The average plots, however, may oversimplify the grain size and circularity data, excluding some of the important extreme values. The bubble aspect ratio averages show a good comparison.

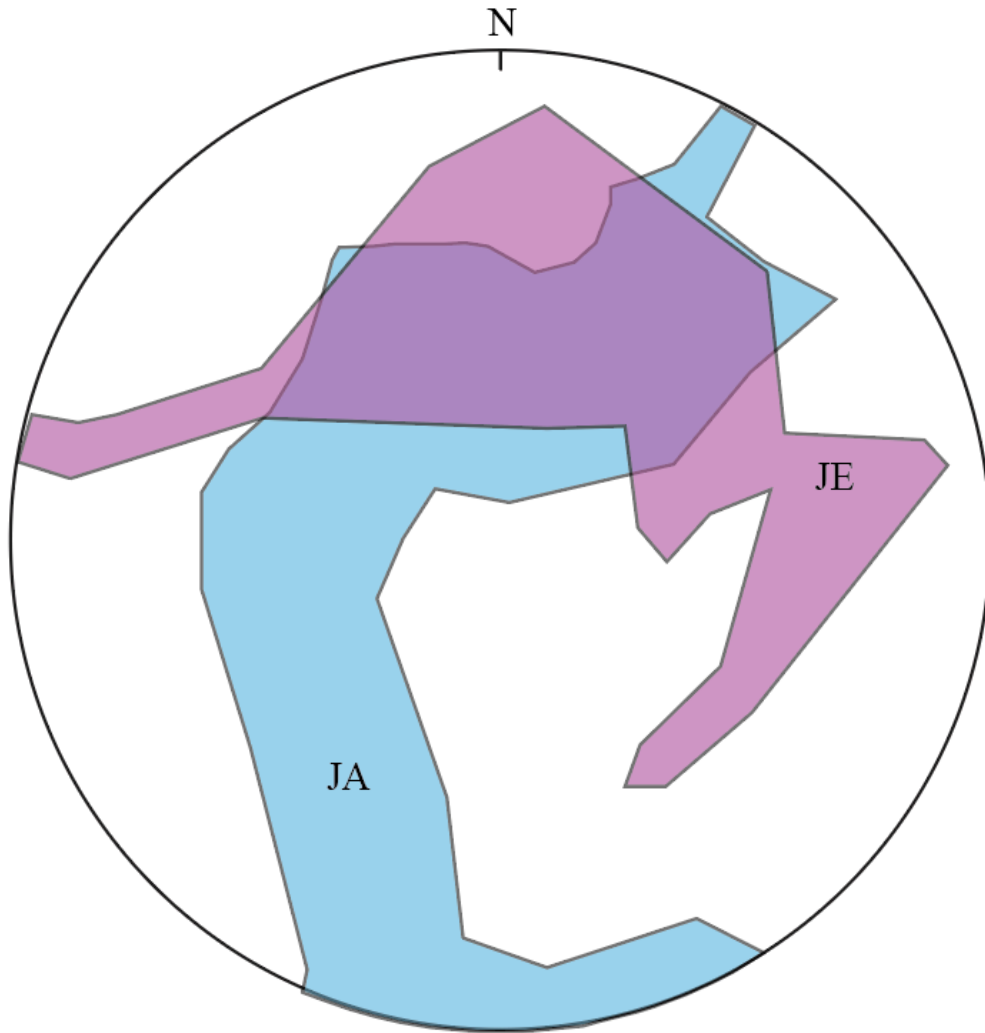


Figure 28

Same stereographic projection as Fig.6, but points have been removed and the areas of distributions in each core were outlined in Adobe Illustrator. The blue shows JA structures and pink is JE. The north direction is labeled "N".

Implications for Glacier Mechanics

Grain size provides a complicated story for studying strain and flow mechanics in a glacier. Grain size is a function of temperature, as well as grain and subgrain processes such as dynamic recrystallization and grain boundary area reduction (GBAR). Strain produces smaller ice crystals; however older ice, found deeper in a core, has larger grains because they had more time to grow and are typically at a higher temperature. JA, overall, has the smallest grains. According to the mean grain size data, JE has the second largest, and JB the largest. It is possible that a small number of thin sections in core JB drove up the average grain size for the whole core. Because core JA is located closer to the center of flow, and is therefore impacted less by shear stress from the lateral margin than JE, I would expect the largest grains. Also, JA is a significantly longer core than both JB and JE, yet there isn't a clear correlation between grain size and depth, and JB/JE still have larger grains. The standard deviations for core JB are also greater. Also, JA and JB were drilled approximately 25m away from each other, so I would expect less variance between JA and JB than exists, and more between JE. This may indicate that grain size itself involves too many factors to conclude anything detailed about glacier mechanics, other than that heterogeneity exists.

Intrahole comparisons for grain size show little heterogeneity for cores JA and JB, with slightly more variation in core JE. This indicates a lack of vertical strain gradients in this region of Jarvis. However, since grain size should increase with depth, it may indicate that there is more strain deeper, resulting in the grains being more unified throughout the core. This could potentially be due to increased shear stress deeper in the glacier from the bed.

Grain circularity is a function of strain and grain boundary area reduction, which affects the perimeter length of a grain. Since ice crystallizes similarly to quartz, ideally forming hexagonal grains, we can compare grains with the circularity value of a hypothetical hexagon. ImageJ uses the equation: $4\pi A/P^2$ (A = Area and P = Perimeter) to calculate circularity. If a hypothetical hexagon had a side length of 1cm, the area would be approximately 2.6cm^2 and perimeter, 6cm. Using the ImageJ equation, a perfect hexagon would have a circularity value of 0.9. As expected, all of the grains fall below this value. Core JA, however, has grains with the greatest circularity values, with JB following, and JE with the lowest. Grain circularity close to a value of 0.9 would imply less deformation occurred, or that the ice crystals had sufficient time to reduce irregular edges. Unfortunately, there are no datasets that would have past ice velocity and velocity gradients to conclude that it was the result of time after deformation, although higher grain circularity in JA correlates with it being closer to the center of flow.

Elongated bubbles and the orientation of their major axes provide perhaps the clearest picture of strain. Grain size and circularity are impacted by other factors besides strain, such as temperature and various grain crystal processes. Therefore they are much more complicated. All three cores have consistent intracore bubble shapes. The histograms, line graphs, and averages all show that JA and JB have smaller aspect ratios, with JE having the largest. JE was drilled about 100m closer to the lateral margin of Jarvis glacier than JA and JB, meaning there would be greater resistance to flow and larger strain resulting in more elongated bubbles oriented in the same direction. The Stereonet graphs show that most bubbles have the same orientation in JE, (Fig.9), but bimodal distributions in JA and JB, (Fig.7,8). Bubble characteristics may indicate either

more strain at JE than the other two cores, or more cohesive strain. Overall, this implies lateral strain gradients across Jarvis Glacier.

CONCLUSIONS

According to the line graphs, intrahole heterogeneity is most prominent in grain circularity for all three cores. Variations between thin sections for grain size in cores JA and JB were insignificant, while JE had slightly more variability. Bubble shape data had small inconsistencies between thin sections. The lack of intrahole heterogeneity among the dipping debris bands and refrozen cracks show that they formed either under similar conditions or that there were insignificant vertical mechanical gradients.

Comparing ice cores against one another provides insight into horizontal gradients. Across the cores, there is heterogeneity among grain size, shape, bubble shape, orientation, as well as dip orientations in debris bands and cracks. Grain size and circularity cannot be directly attributed to a singular flow process. Therefore, clear conclusions cannot be made regarding why they are sized and shaped a certain way, and what this says about the flow. The most important takeaway from these data, however, is that there is heterogeneity in these measurements between cores. Dip orientation and angles for the debris bands and refrozen fractures show different behavior in core JA than in JE, which indicated mechanical differences between the two cores.

Out of all microstructure elements measured, bubble aspect ratio and orientations provide a clear picture of how strain varies from the lateral margin towards the center of flow. Intrahole consistency suggests that mean aspect ratios are sufficient for larger scale comparisons. In all graphs, JE shows significantly higher aspect ratios than cores JA and JB. Also, almost all bubbles are oriented around 90° on the stereonet plot. Most likely due to its proximity from the margin, and assuming bubbles can be used as strain indicators, core JE has undergone the greatest strain out of the three cores.

In conclusion, this microstructural analysis shows that there is heterogeneity among grain and bubble properties. With this, flow models that rely on uniformly deforming ice, and homogenous microstructure, should be re-evaluated. Creating flow laws and models that more closely adhere to mechanics as a result of the material properties of ice may help us predict glacier flow more accurately as ice loss continues.

REFERENCES

1. B. Alley, I. Joan, Conditions for bubble elongation in cold ice-sheet ice. **45** (1994).
2. R. W. Baker, The Influence of Ice-Crystal Size on Creep. *J. Glaciol.* (1978).
3. R. S. Bradley, M. Vuille, H. F. Diaz, W. Vergara, Threats to Water Supplies in the Tropical Andes. *Science* (80-.). **312**, 1755–1757 (2006).
4. K. Cuffey, W. S. B. Paterson, *The Physics of Glaciers* (2010).
5. S. H. Faria, I. Weikusat, N. Azuma, The microstructure of polar ice . Part I : Highlights from ice core research. *J. Struct. Geol.* **61**, 2–20 (2014).
6. J. M. Fegyveresi, R. B. Alley, D. E. Voigt, J. J. Fitzpatrick, L. A. Wilen, Instruments and methods : a case study of ice core bubbles as strain indicators. **60**, 8–19 (2019).
7. pp. 817-823. Gleick, P. H., 1996: Water resources. In Encyclopedia of Climate and Weather, ed. by S. H. Schneider, Oxford University Press, New York, vol. 2, No Title.
8. J. . Glen, The Creep of Polycrystalline Ice, 519–538 (1954).
9. M. J. Hambrey, Debris, Bubble, and Crystal Fabric Characteristics of Foliated Glacier Ice, Charles Rabots Bre, Okstindan, Norway Michael. *Arct. Alp. Res.* (1976).
10. R. L. Hooke, Flow Law for Polycrystalline Ice in Glaciers: Comparison of Theoretical Predictions, Laboratory Data, and Field Measurements. *Rev. Geophys. Sp. Phys.* **19**, 664–672 (1981).
11. P. J. Hudleston, in *Energetics of Geological Processes* (1977), pp. 121–150.
12. P. J. Hudleston, Structures and fabrics in glacial ice : A review. *J. Struct. Geol.* **81**, 1–27 (2015).
13. K. R. Miner *et al.*, Organochlorine Pollutants within a Polythermal Glacier in the Interior Eastern Alaska Range. *Water*, 1–14 (2018).
14. M. Nakawo, Gorow Wakahama, Preliminary Experiments on the Formation of Elongated Air Bubbles in Glacier Ice by Stress. *J. Glaciol.* **27** (1981).

15. C. W. Passhler, R. A. J. Trouw, *Microtectonics* (Springer-Verlag, Berlin, Germany, 1996).
16. L. Placidi, R. Greve, H. Seddik, Continuum-mechanical , Anisotropic Flow model for polar ice masses , based on an anisotropic Flow Enhancement, 221–237 (2010).
17. M. Song, I. Baker, D. M. Cole, The effect of particles on creep rate and microstructures of granular ice. **54**, 533–537 (2008).
18. M. Song, D. M. Cole, I. Baker, Initial experiments on the effects of particles at grain boundaries on the anelasticity and creep behavior of granular ice, 397–401 (2004).
19. I. M. Whillans, C. J. Van Der Veen, The role of lateral drag in the dynamics of Ice Stream B, Antarctica. *J. Glaciol.* **43** (1997).
20. M. Zemp *et al.*, Global glacier mass changes and their contributions to sea-level rise from 1961 to 2016 (2017), doi:10.1038/s41586-019-1071-0.

APPENDIX

TABLE OF MEAN GRAIN SIZE, GRAIN CIRCULARITY,
AND BUBBLE ASPECT RATIO

Core	Depth (m)	Mean Grain Size (mm ²)	Mean Grain Circularity	Mean Bubble Aspect Ratio
JE	0.60	68.24	0.51	1.52
JA	4.41	3.29	0.60	1.37
JE	6.87	40.08	0.55	1.88
JE	7.53	32.79	0.59	1.88
JE	9.64	6.34	0.60	1.67
JE	13.61	57.06	0.53	1.54
JA	14.29	1.98	0.65	---
JB	14.79	3.10	0.64	1.47
JE	15.60	65.18	0.54	1.65
JB	16.07	154.73	0.53	1.19
JB	19.14	14.58	0.61	1.22
JA	20.85	2.23	0.65	1.23
JB	22.55	59.31	0.55	1.22
JB	23.95	92.05	0.59	1.25
JB	25.54	117.57	0.56	1.19
JA	25.76	20.19	0.58	1.27
JB	26.15	388.92	0.56	1.20
JA	36.07	2.29	0.64	1.39
JA	46.82	22.25	0.53	1.27
JA	52.23	17.98	0.61	---
JA	54.76	4.00	0.63	---
JA	57.20	2.29	0.63	1.37
JA	58.61	20.20	0.59	1.18
JA	59.00	3.80	0.61	1.16
JA	60.43	10.92	0.64	1.30
JA	65.63	9.76	0.63	1.32
JA	71.98	94.62	0.51	1.24

Table 2

Table displaying the mean grain size, grain circularity, and bubble aspect ratio compared with depth in the ice core and which core the measurements are from.

AUTHOR'S BIOGRAPHY

Renée Clavette is from South Berwick, ME. She is graduating with a Bachelor of Science in Earth and Climate Sciences with a concentration in Climate Science in May of 2020. Throughout her time at the University of Maine she was a part of the Geology Club and the Tennis Club, which she was president of for 3 years. When she isn't studying or doing research, Renée can be found hiking, playing tennis, practicing piano, and overall appreciating the Maine outdoors, whether it be boating and fishing in the St. John Valley, skiing at Sugarloaf, hiking in Baxter State Park, or walking along the coast. This coming fall she will be entering into a glaciology Master's program in the School of Earth and Atmospheric Sciences at the Georgia Institute of Technology in Atlanta. She hopes her future studies bring her to many different places, studying the world's glaciers.